Crystallography of refractory metal nuggets in carbonaceous chondrites

Luke Daly[a,*], Phil A. Bland[a], Kathryn A. Dyl[a], Lucy V. Forman[a], Patrick W. Trimby[b], Steve Moody[b], Limei Yang[b], Hongwei Liu[b], Simon P. Ringer[c], Martin Saunders[d], Sandra Piazolo[e]

[a]*Department of Applied Geology, Curtin University, GPO Box U1987, Perth, WA* 6845*, Australia.*
[b]*Australian Centre for Microscopy and Microanalysis, The University of Sydney, NSW* 2006*, Australia.*
[c]*Australian Institute for Nanoscale Science and Technology, and School of Aerospace, Mechanical and Mechatronic Engineering, The University of Sydney, NSW,* 2006*, Australia.*
[d]*Centre for Microscopy, Characterisation and Analysis, The University of Western Australia, WA* 6009*, Australia.*
[e]*Department of Earth and Planetary Sciences, Macquarie University NSW,* 2109*, Australia.*

Abstract

Transmission Kikuchi diffraction (TKD) is a relatively new technique that is currently being developed for geological sample analyses. This technique utilises the transmission capabilities of a scanning electron microscope (SEM) to rapidly and accurately map the crystallographic and geochemical features of an electron transparent sample. TKD uses a similar methodology to traditional electron backscatter diffraction (EBSD), but is capable of achieving a much higher spatial resolution (5-10 nm). Here we apply TKD to refractory metal nuggets (RMNs) which are micrometre to sub-micrometre metal alloys composed of highly siderophile elements (HSEs). TKD allows us to analyse RMNs *in situ*, enabling characterisation of nanometre-scale variations in chemistry and crystallography, whilst preserving their spatial and crystallographic context. This provides a complete representation of each RMN, permitting detailed interpretation of their formation history.

We present TKD analysis of five transmission electron microscopy (TEM) lamellae containing RMNs coupled with EBSD and TEM analyses. These analyses revealed textures and relationships not previously observed in RMNs. These textures indicate RMNs have experienced annealing, forming twins. RMNs can also act as nucleation centres, as well as form immiscible metal-silicate fluids. In fact, each RMN analysed in this study has different crystallographic textures. These RMNs also have heterogeneous compositions, even between RMNs contained within the same inclusion, host phase and even separated by only a few micrometres. One sample has textures consistent with the formation of two immiscible melts: metal and silicate, consistent with expected textures associated with precipitation of HSEs from a silicate melt as suggested by Schwander et al. (2015b). However, most RMNs have crystallographic textures indicating that the RMN formed prior to their host inclusion. TKD analyses reveal most RMNs have been substantially affected by processing in the protoplanetary disk. Despite this alteration, RMNs still preserve primary crystallographic textures and heterogeneous chemical signatures. This heterogeneity in crystallographic relationships, which mostly suggest that RMNs pre-date their host, is consistent with the idea that there no a dominant RMN forming process. Each RMN has experienced a unique history, supporting the suggestion

*Corresponding author: Luke Daly, Email: luke.daly@postgrad.curtin.edu.au, telephone: +61497840194

of Daly et al. (in review), that RMNs may preserve a diverse pre-solar chemical signature inherited from the Giant Molecular Cloud.

Keywords: `Refractory Metal Nuggets, Solar Nebula, Solar System, Origin, Meteorites, carbonaceous chondrites, crystallography, crystallisation, Transmission Kikuchi diffraction`

1. Introduction

Refractory metal nuggets (RMNs) are metal alloys composed of highly siderophile elements (HSEs). Since their co-discovery by Palme & Wlotzka (1976) and Wark & Lovering (1976), it had been assumed that they are only found in Ca-Al rich inclusions (CAIs) (Blander et al., 1980; Berg et al., 2009; Harries et al., 2012; Hewins et al., 2014). However, observations of RMNs in chondrules (Wang et al., 2007) and matrix (Schwander et al., 2015a) as well as recent X-ray fluorescence microscopy (XFM) synchrotron data, have revealed that this is not the case. Daly et al. (in review) showed that RMNs are found within all components of carbonaceous chondrites. The assumption that RMNs were hosted solely within refractory inclusions has meant that formation mechanisms were only considered within the context of CAIs. This lead to the conclusion that RMNs are primary condensates (Berg et al., 2009; Fegley & Palme, 1985; Grossman, 1973; Harries et al., 2012; Lodders, 2003; Palme & Wlotzka, 1976). Recent work by Schwander et al. (2015a) and Rudraswami et al. (2014) respectively has shown that this is not necessarily the case: an alternative mechanism may be precipitation of RMNs from a silicate melt, CAI-like fluid, or during the formation of cosmic spherules. Furthermore, RMNs have, in some cases, been subjected to secondary processes as implied by sulphidation and oxidation textures (Bischoff & Palme, 1987; Blum et al., 1988; Palme & Wlotzka, 1976). However, other studies have suggested that RMNs may have a pre-solar origin (El Goresy et al., 1977, 1978; Wark & Lovering, 1976). This was confirmed by recent observations of $20 - 50$ nm RMNs hosted within pre-solar graphite (Croat et al., 2013).

A combination of 113 *in situ* energy-dispersive X-ray spectroscopy (EDS) measurements of RMNs and the database of RMNs reported in the literature over the last 40 years, revealed a large range of RMN compositions which cannot be reconciled by a single Solar System process (Daly et al., in review). Our interpretation is that an inherently diverse population of RMNs was incorporated into the protoplanetary disk. These RMNs were altered by subsequent disk processing, but the primordial diversity was never overprinted (Daly et al., in review).

The crystallography of RMNs can offer important insights into their origin and formation. For example, the three phase condensation model of Sylvester et al. (1990) predicted that RMNs should be found in three main crystal systems: body centred cubic (bcc) composed predominantly of W, Mo, and Cr; hexagonal close packed (hcp) composed predominantly of Re, Os, and Ru; and a face centred cubic (fcc) structure composed of Ir, Pt, Rh, Co, Ni, Fe, and Au. This assertion was proposed to reconcile RMN compositions that do not fit a single-phase condensation model. However, the observed crystallography of RMNs using transmission

electron microscopy (TEM) spot diffraction patterns indicate that they are largely monocrystalline, homogeneous, subhedral-euhedral hcp crystals (Eisenhour & Buseck, 1992; Harries et al., 2012; Croat et al., 2013). This observation does not support the three phase condensation model, and reinforces the idea of a single phase equilibrium condensation origin for RMNs, in agreement with calculations by Campbell et al. (2001) and Wark & Lovering (1976). However, the chemical heterogeneity of RMNs is still not fully understood. Previous work has either been limited to analysis of a few grains *in situ* (Blum et al., 1988; El Goresy et al., 1978; Palme & Wlotzka, 1976; Wark, 1986; Wark & Lovering, 1976), or analysis of many grains using acid residues (Berg et al., 2009; Harries et al., 2012; Schwander et al., 2014) where the original context of the RMN was lost. Two studies have analysed significant quantities of RMNs *in situ* (Daly et al., in review; Schwander et al., 2015b). Schwander et al. (2015b) demonstrated that the condensation temperature of the host mineral phase did not correlate with appropriate RMN compositions if RMNs had formed as condensates, implying that condensation was an unlikely formation mechanism for RMNs in that study.

Analyses of inclusion-host systems in terrestrial rocks using large electron backscatter diffraction (EBSD) datasets, and the documentation of crystallographic orientation relationships (CORs) between mineral phases by Griffiths et al. (2016) revealed variable CORs between mineral inclusions and their host phase correlate with changing metamorphic conditions. The context of the RMN is integral to the accurate interpretation and discernment of mineral formation mechanisms, as the formation history of the host itself will influence the interpretation. For example, RMNs hosted within chondrules which are not thought to have a condensation history, may indicate that these RMNs formed via a different mechanism. Also, any secondary alteration events experienced by the host phase would necessarily affect the RMN and may influence its crystallography and composition.

To determine which processes have affected RMNs since their formation, high resolution *in situ* analyses are required. Transmission Kikuchi diffraction (TKD) is a relatively new technique and its applications to geological (Jacob et al., 2016; Piazolo et al., 2016) and meteoritical samples (Forman et al., 2016) are beginning to be explored. The technique allows the elemental and crystallographic mapping of a TEM lamella in a scanning electron microscope (SEM). It uses the same software and techniques as EBSD, but with an order of magnitude improvement in the resolution attainable (Trimby, 2012; Trimby et al., 2014; Sneddon et al., in review). This approach allows us to observe RMNs in context, preserving any CORs with associated host phases, and rapidly map the crystallography of these grains at ~ 5 nm resolution. It therefore provides a completely new window on the crystallography, orientation, and deformation history of these materials that has not been accessible before. TKD analysis can facilitate better interpretation of the sequence of events that may have affected each RMN since formation, and how these processes may have affected the RMNs crystallography and chemistry.

The only other study utilising TKD on meteoritic materials by Forman et al. (2016) demonstrated that TKD can be used to highlight the differences in how matrix and chondrules are affected by temperature and stress during impact induced compaction in the matrix of Allende near a chondrule. Here we will

further demonstrate the potential of this technique in the analysis of RMNs. We will show and explore the possible observable effects on the crystallography and chemistry, produced by primary nebula processes, i.e. condensation and crystallisation; secondary nebular processes, i.e. transient heating events; and secondary asteroidal processes, i.e. sulphidation. TKD observations are supplemented with the utilisation of established techniques, such as EBSD and TEM.

2. Methods

To identify RMNs *in situ*, a combination of Synchrotron XFM analyses corroborated with SEM observations using map overlay and feature mapping software packages. A full description of the procedure can be found in (Daly et al., in review). Several RMN bearing regions were identified for analysis in this study: Region A1, a sulphide nodule hosted within a chondrule in Allende; A2, a forsterite inclusion hosted in a CAI in Allende; A3, a forsterite inclusion in another CAI in Allende; ALH1, a type B-like CAI in ALH 77307; and V1 and V2 from the reheated portion of a fluffy type A CAI in Vigarano. Regions A1 and A3 were analysed using EBSD techniques. Regions A1, A2, ALH1, V1, and V2 were extracted and analysed using TKD, and region ALH1 was also analysed using TEM.

2.1. EBSD

The samples were prepared for EBSD by hand polishing for 30 minutes using 0.01 µm colloidal silica in NaOH solution. This reduces the risk of polishing away the micrometre sized RMNs identified on the surface whilst achieving the polish required for EBSD. The samples were then coated with 10 nm of carbon. EDS and EBSD data were collected using the Zeiss ULTRA Plus Field emission gun (FEG) SEM at the Australian Centre for Microscopy and Microanalysis (ACMM), The University of Sydney, with an X-Max 20mm^2 SDD EDS detector at an accelerating voltage of 20 kV.

2.2. Focussed Ion Beam

The samples A1, A2, ALH1, V1, and V2 were extracted and prepared for TEM and TKD using a focussed ion beam (FIB) on the Zeiss Auriga FIB-SEM at the ACMM, The University of Sydney. The regions of interest were initially covered with a protective strip of Pt using secondary electrons, followed by a thicker layer deposited using the Ga beam. This procedure is to protect the sample during milling, and thinning, while also adding structural support to the lamellae. The section was extracted using a Kleindiek micromanipulator, and welded to a Cu TEM grid with further Pt deposition. The sample was then thinned to approximately 100 nm thickness to allow the transmission of electrons.

2.3. TKD

The samples A1, A2, ALH1, V1, and V2 were analysed using TKD on the Zeiss ULTRA Plus FEG SEM at the ACMM, The University of Sydney. TKD mapping was performed using a Nordlys-NANO EBSD

detector, and EDS maps were collected with an X-Max 20 mm^2 SDD EDS detector using an acceleration voltage of 30 kV as described in Trimby (2012) and Trimby et al. (2014).

2.4. Data reduction

The EDS, EBSD and TKD maps were collected and interpreted using the Oxford instruments AZtec and Channel 5 software packages. Grain boundaries were defined by >10 degree misorientation. Element abundances were derived from the EDS maps using standardless quantitative methods embedded in the Aztec software. EDS measurements of RMNs were taken with a process time of 5. This allows for better energy resolution and detection limits. The L-alpha X-Ray lines were used to calculate elemental abundances for Ru, Mo, W, Re, Os, Ir and Pt, as these are better separated than the M lines. K X-ray lines were used to calculate Fe and Ni abundances. Detection limits for elements within RMNs were approximately <1 At%. The relative uncertainty in these measurements is approximately ± 10 % . This provides sufficient accuracy to detect major and minor elements and draw comparisons between measured RMN compositions in different meteoritic components. All other elements present in the spectra such as Mg, Al, Ca, Cu etc; were ignored, as they are likely to be generated by fluorescence in the SEM chamber from elements in the surrounding phases, or the sample mount. We do not expect these elements to be present in RMNs. RMNs were mostly characterised by a fcc awaruite or a hcp rutheniridosmin crystal structure from the EBSD database as the phase that best described most RMNs observed.

2.5. TEM

The FIB lamella taken from ALH 77307 (region ALH1) was also analysed using the JEOL2200 TEM, ACMM, the University of Sydney and the FEI Titan G280 − 200 TEM/STEM, Centre for Microscopy, Characterisation and Analysis (CMCA), University of Western Australia at an accelerating voltage of 200 kV. The sample was mounted on a double-tilt sample holder allowing the sample to be tilted in two directions. This allows greater flexibility to find and identify crystallographic axes. High resolution EDS maps, spot diffraction patterns and high resolution TEM (HRTEM) images were collected.

3. Results

3.1. Allende - region A1

This RMN bearing region revealed RMNs hosted within a pentlandite nodule. Three RMNs were observed on the surface in the EBSD dataset (Figure 1), while a further five RMNs were revealed during the TKD analyses that were previously buried beneath the surface of the sample (Figure 2). The RMNs varied in size from 0.1 µm to 1 µm, and form anhedral-subhedral fcc single crystals. The RMNs had identical CORs relative to each other (Figures 1 and 2). The RMNs have no COR with the pentlandite host phase, however, they do share a [100] axis with the nearby forsterite crystal (Figure 1 and 2). Three RMNs from the EBSD dataset (Table 1) and four from the TKD dataset (Table 2) were large enough to generate good EDS spectra.

The composition of the RMNs indicated that in most cases Fe and Ni are relatively homogeneous between RMNs, with the exception of entry # 3 in Table 2. Fe and Ni were significantly overestimated in the EBSD dataset as the interaction volume of the EDS measurement was significantly larger than the RMN. This means that there was a significant contribution to the EDS spectra from the surrounding pentlandite. The HSE elements Ir and Pt vary significantly (Tables 1 and 2). The Pt should be interpreted with caution as there was likely to be some contribution of Pt from the fluorescence of the Pt protective layer deposited during FIB sample preparation in the EDS spectra in Table 2. However, the EDS spectra from the EBSD dataset (Table 1) confirms that Pt is present and variable. Mo and W are completely absent in all RMNs in this region and Os is only observed in RMN 2 in Table 2).

Table 1: RMN compositions from EDS analysis from Figure 1. The RMN number relates to the numbered regions of Figure 1b. b.d. = below detection.

RMN	At%			
	Fe	Ni	Ir	Pt
1	66.1	25.8	6.8	1.3
2	61.3	32.9	b.d.	5.8
3	62.4	27.8	2.1	7.8

Table 2: RMN compositions from EDS analysis from Figure 2. The RMN number relates to the numbered regions of Figure 2c. b.d. = below detection.

RMN	At%				
	Fe	Ni	Os	Ir	Pt
1	13.2	10.9	b.d.	6.1	69.8
2	12.9	10.1	2.1	16.3	58.5
3	15.5	37.7	b.d.	46.8	b.d.
4	12.4	10.8	b.d.	20.2	56.7

3.2. Allende - region A2

The TEM lamellae extracted from Allende - region A2: a forsterite inclusion in a CAI. When analysed using TKD revealed a cluster of RMNs with two distinct morphologies. The first was a large polycrystalline RMN associated with molybdenite. The second was several isolated smaller RMNs ($20 - 100$ nm). These smaller RMNs were single crystals with a spherical morphology hosted in forsterite. The whole inclusion was surrounded by spinel (Figure 3). All RMNs here had a hcp stucture and uniform chemistry in relation to Ru, Ir and Pt. They were also completely devoid of Mo which was situated in the molybdenite (Table 3). The molybdenite and the larger polycrystalline RMN were crystallographically aligned with each other.

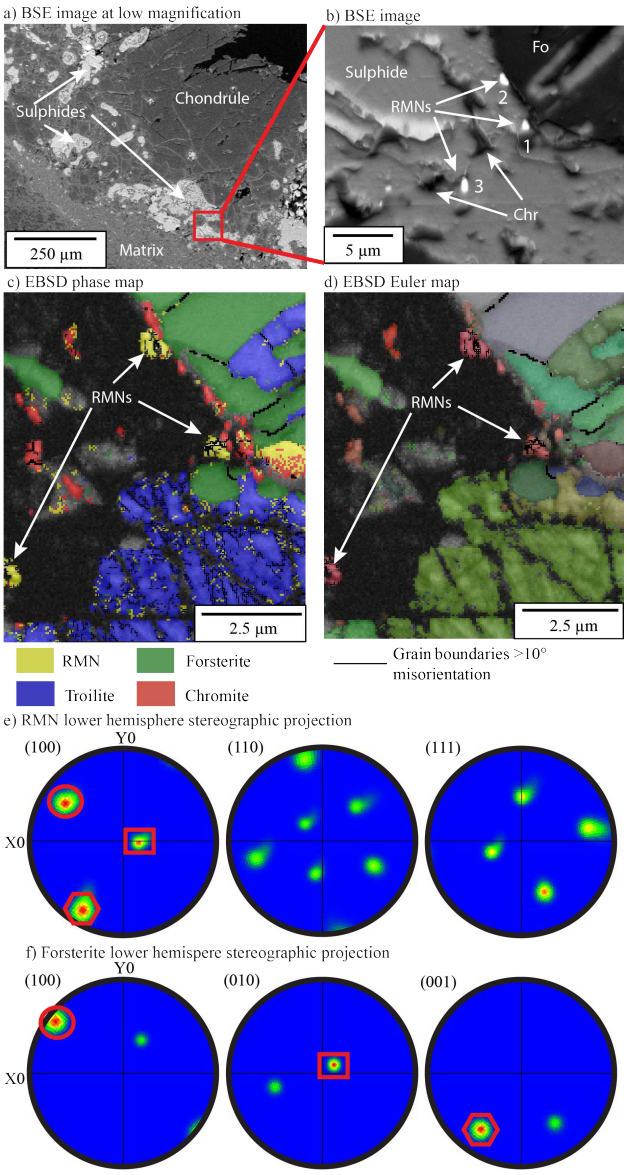

Figure 1: Characteristics of Allende - region A1: EBSD analyses of 3 RMNs are contained within a chondrule-hosted sulphide nodule. a) A low magnification back scatter electron (BSE) image of region A1, indicating the wider context of the chondrule host with associated sulphide nodules, b) A BSE image of the RMNs hosted within a sulphide, with a nearby forsterite grain (Fo) as well as associated chromite inclusions (Chr). The numbers indicate where the EDS measurements were taken from in Table 1, c) An EBSD phase map overlain on a band contrast image indicating RMNs (yellow), troilite (blue) chromite (red) and forsterite (green), the pentlandite sulphide did not index well and is located within the black area, d) An EBSD Euler image overlain on a band contrast image indicating crystallographic orientations of each phase, e) A lower hemisphere stereographic projection of RMN crystallographic axes (100), (110), and (111). The crystallographic orientations of the RMNs revealed all RMNs have the same crystallographic alignment, f) A lower hemisphere stereographic projection of the orientation of the forsterite crystallographic axes (100), (010), and (001). The red square, circle and hexagon on stereographic projections e) and f) indicate that the RMNs and the forsterite share a [100] axis.

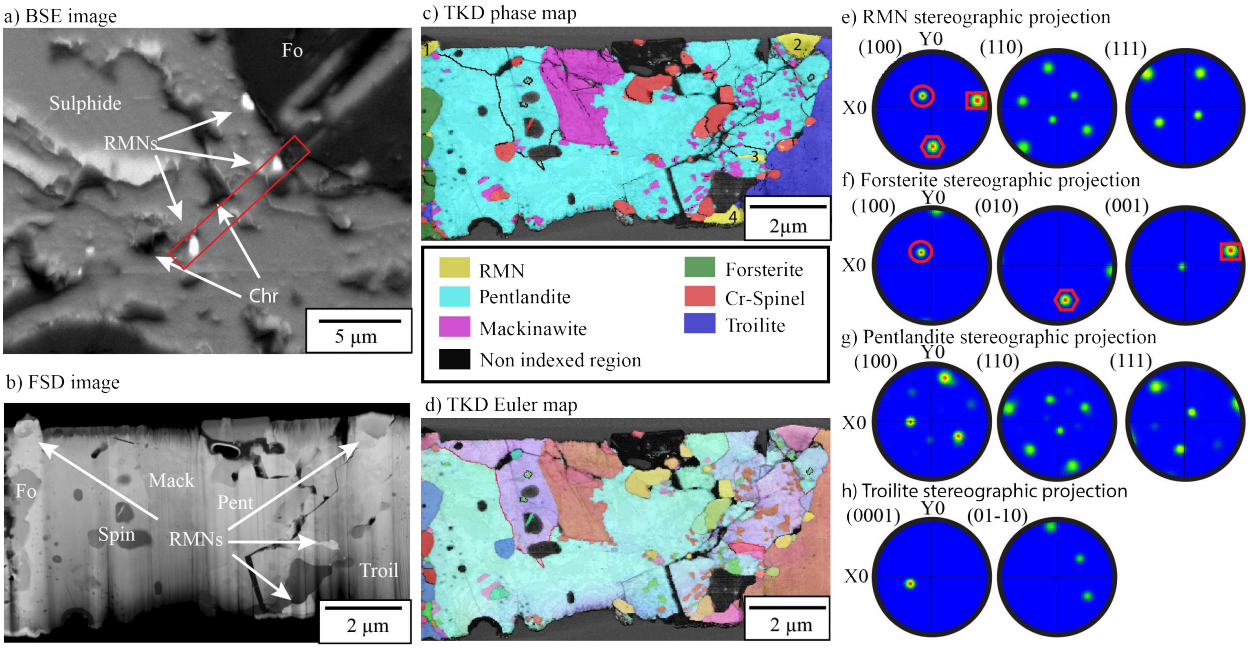

Figure 2: Characteristics of Allende - region A1: TKD analyses from a FIB-produced TEM lamellae containing an RMN bearing sulphide nodule hosted in a chondrule. a) A BSE image of the RMNs in context prior to extraction. The TEM lamellae was extracted as indicated by the red rectangle. Associated minerals are forsterite (Fo), chromite (Chr) and sulphide, b) A TKD fore-scatter detector (FSD) image of the TEM lamellae RMNs and associated minerals are labelled forsterite (Fo), mackawininte (Mack), spinel (Spin), pentlandite (Pent) and troilite (Troil), c) TKD phase map, revealing five more RMNs (yellow) which were buried beneath the surface of the sample, the numbers relate to EDS measurements detailed in Table 2, d) TKD Euler map showing crystallographic orientations of each phase in the section, e) Lower hemisphere stereographic projection of crystallographic orientations of the RMNs revealed a consistent crystallographic orientation for all RMNs, f) Lower hemisphere stereographic projection of crystallographic orientations of the forsterite confirming a shared [100] axis between the RMNs and forsterite observed in Figure 1, denoted by the red circle square and hexagon, g) Lower hemisphere stereographic projection of crystallographic orientations of pentlandite, indicating no COR between the RMN and the pentlandite h) Lower hemisphere stereographic projection of crystallographic orientations of the troilite, indicating no COR between the RMN and the troilite.

They also exhibit a higher misorientation density, whereas the forsterite and smaller RMNs are uniform
150 single crystals. The surrounding spinel was equigranular (2-5 µm) with 120° grain boundary intersections.

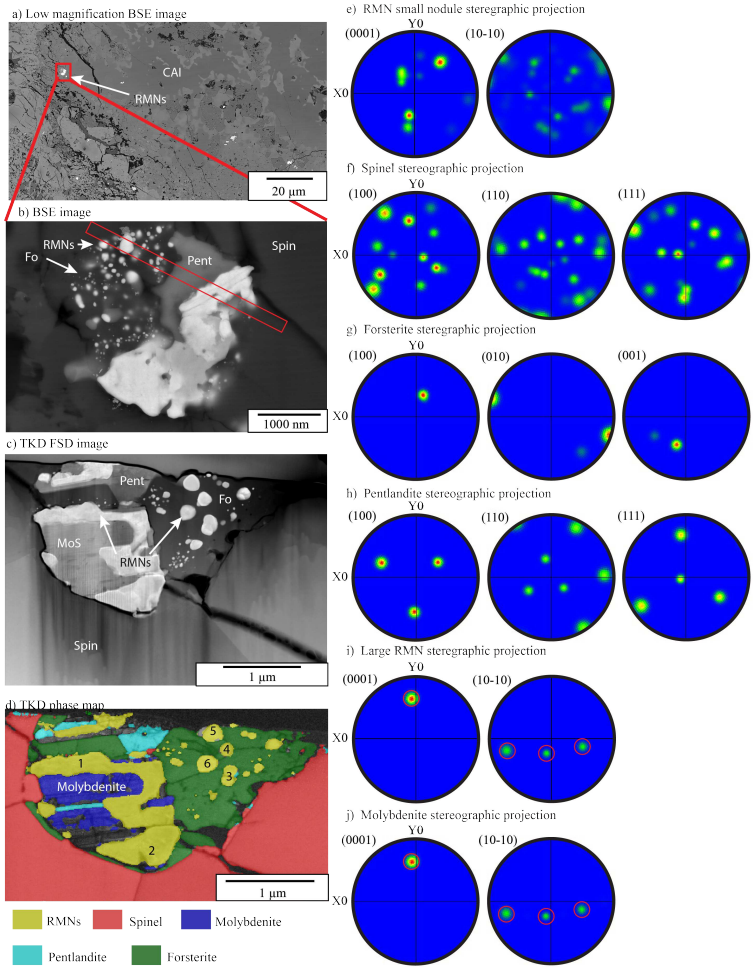

Figure 3: Characteristics of Allende region A2: TKD analyses from a FIB-produced TEM lamellae of an RMN-bearing forsterite inclusion hosted in a CAI. a) A low magnification BSE image of region A2 indicating the wider context of the CAI host, b) A BSE image of the RMNs (bright spots) in context prior to extraction. The TEM lamellae was extracted as indicated by the red rectangle. RMNs and associated minerals were labelled forsterite (Fo), pentlandite (Pent), and spinel (Spin), c) A FSD image of the TEM lamellae indicating the RMN bearing region at the top and revealing the surrounding spinel's 120° grain boundary intersections and $2-5$ µm grain size. RMNs and associated minerals are labelled forsterite (Fo), pentlandite (Pent), molybdenite (MoS), and spinel (Spin), d) TKD phase map, revealing an large RMN associated with molybdentite and smaller spherical RMNs suspended in forsterite. The numbers relate to EDS measurements in Table 2. The whole inclusion is encapsulated by spinel, e) Lower hemisphere stereographic projection of crystallographic orientations of the small RMN spheres revealing random crystallogrpahic orientations for each RMN relative to each other, f) Lower hemisphere stereographic projection of crystallographic orientations of the spinel, g) Lower hemisphere stereographic projection of crystallographic orientations of the forsterite, h) Lower hemisphere stereographic projection of crystallographic orientations of the pentalndite, i) Lower hemisphere stereographic projection of crystallographic orientations of the large RMN, j) Lower hemisphere stereographic projection of crystallographic orientations of molybdentite. The molybdenite and the large RMN are crystallographically aligned parallel to one another as the indicated by the red circles in i) and j).

Table 3: RMN compositions from EDS analyses from the TEM lamellae detailed in Figure 3. The RMN number relates to the numbered regions of Figure 3c. b.d. = below detection.

Spectrum Label	At %						
	Fe	Ni	Mo	Ru	Os	Ir	S
Molybdenite	0.9	b.d.	33.5	b.d.	b.d.	b.d.	65.6
1	10.9	b.d.	3.6	44.6	22.9	18.0	b.d.
2	12.5	b.d.	2.4	44.3	23.6	17.2	b.d.
3	13.7	b.d.	b.d.	41.9	26.7	17.7	b.d.
4	13.1	b.d.	b.d.	40.1	26.1	20.7	b.d.
5	11.9	b.d.	b.d.	41.6	26.4	20.0	b.d.
6	15.2	b.d.	b.d.	38.4	28.0	18.4	b.d.

3.3. Allende - region A3

Here an RMN hosted within a forsterite inclusion contained within augite from a CAI in Allende was observed. EBSD analyses revealed that the RMN has a COR with forsterite, sharing the [110] axis (Figure 4).

Table 4: RMN compositions from EDS analyses from Figure 4. The RMN number relates to the numbered regions of Figure 4c. b.d. = below detection.

RMN	At%					
	Fe	Ni	Ru	Mo	Os	Ir
1	21.5	5.3	50.4	3.8	4.5	14.6

3.4. ALH 77307 - region ALH1

TKD and TEM analyses of region ALH1, an extracted RMN from a type B-like CAI in ALH 77307, revealed a single RMN hosted within a $40 - 60$ % åkermanite-gehlenite host. The RMN is also associated with a probable new mineral phase. As the new mineral phase had not previously been documented, no mineral EBSD data were available to index it. Therefore a proxy of Fe_7W_6 with space group 166 and $a = b = 0.4731$ nm and $c = 2.57$ nm was used. This mineral has a trigonal crystal structure and a very long c axis relative to the a and b axes. Using this proxy and TEM spot diffraction, this phase was revealed to be closely related to the trigonal Fe_7W_6 proxy with $a = b = 0.46$ nm $c = 2.55$ nm with space group R-3m (166), and a simplified chemical formula (Fe, Ni)$_6$(Mo, Ru, W, Os, Ir, Pt)$_7$. The ionic radii of all elements were very similar so a more general formula could be (Fe, Ni, Mo, Ru, W, Os, Ir, Pt)$_{13}$. The RMN is fcc and perfectly euhedral. The new phase follows the grain boundary defined by the RMN and the åkermanite-gehlenite host. Which is consistent with a pseudomorph texture (Figure 5). This new mineral

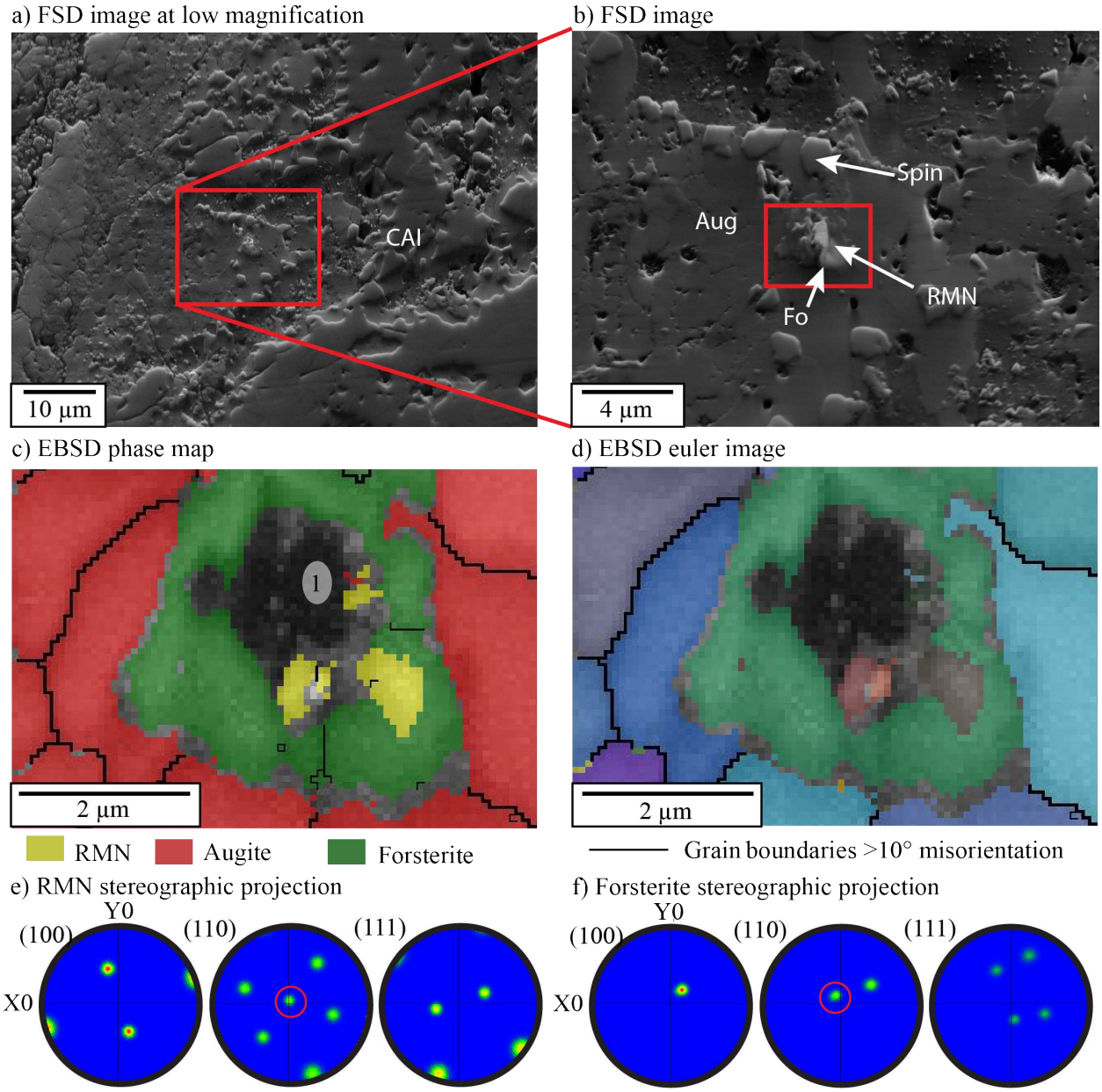

Figure 4: Characteristics of Allende - region A3: EBSD analyses of a forsterite hosted RMN from a CAI. a) A low magnification FSD image of region A3 (red box) indicating the context of the RMN within the CAI, b) FSD image of Region A3 indicating where the EBSD dataset was acquired (red box), associated minerals are labelled forsterite (Fo), spinel (Spin) and augite (Aug), c) EBSD phase map indicating an RMN hosted within a forsterite grain, the number indicates the EDS measurement taken from that point detailed in Table 4, d) Euler map indicating crystallographic orientations, e) Lower hemisphere stereographic projection of crystallographic orientations of the RMN, f) Lower hemisphere stereographic projection of crystallographic orientations of the forsterite. Comparing the projections reveals the RMN have a COR with the forsterite sharing their (110) axis (red circle).

was heavily deformed with elongate bladed crystal growths (Figure 5). TKD supported by TEM analyses indicated that the RMN was crystallographically aligned with the åkermanite-gehlenite host, as the [002] axis of the RMN was oriented parallel to the [201] axis of the åkermanite-gehlenite phase. The RMN was also crystallographically related to the new phase, sharing the same <c> axis to within 6° (Figure 5). The RMN and the new phase had similar abundances of Fe, Ni, Ru, Os and Ir. However, Mo was significantly enriched within the new phase relative to the RMN, and W was present in the new phase but absent from the RMN. Comparing EDS measurements with TKD and TEM indicate that TEM is largely unaffected by Pt fluorescence unlike the TKD measurements. This implies that Pt was only present in the RMN and not in the new mineral phase (Table 5).

Table 5: EDS measurements taken from Region ALH1, comparing TEM with TKD analyses. This label corresponds to the label in Figure 5b. b.d. = below detection.

Technique	Mineral	At%								
		Fe	Ni	Ru	Rh	Mo	W	Os	Ir	Pt
TEM	RMN	55.5	9.4	7.5	b.d.	6.68	b.d.	7.0	4.0	9.9
TKD		46.3	6.7	13.1	3.2	14.8	b.d.	4.7	2.9	8.3
TEM	new mineral	41.5	3.55	8.9	b.d.	35.7	1.7	6.8	2.0	b.d.
TKD		40.0	3.8	9.1	b.d.	38.8	2.0	2.8	1.4	2.0

3.5. Vigarano - region V1

TKD analyses of Vigarano - region V1 revealed a large anhedral 1 µm RMN with a fcc structure associated with an isolated spinel grain to the left of the section. To the right of the section, there was a cluster of 7 RMNs between $0.5 - 0.1$ µm (Figure 6). The cluster of RMNs were euhedral fcc crystals with twinning planes which rotated approximately 60° around the [111] axis with a $20-130$ nm spacing between twin planes (Figure 6). The host phase of the RMNs was anorthite feldspar which was also twinned with a 180° rotation around the twin plane (Figure 6). The composition of each RMN was unique, with variations observed across all elements despite being located in the same inclusion of the same meteorite, and even between the cluster of 7 RMNs exhibiting twinning (Table 6).

3.6. Vigarano - region V2

TKD analyses of Vigarano - region V2 revealed a RMN and associated metal and oxide phases hosted within a spinel grain. The boundary with the spinel and the assemblage exhibited straight edges. The assemblage was subdivided into three phases: a RMN hcp phase, powellite, and awaruite. Each phase was unique in terms of its chemistry, with Mo only found in the powellite, which also exhibited twinning with a rotation about the [111] axis of 60° (Figure 7). Os only occurred in the RMN phase which was also enriched in Ru and depleted in Ni relative to the awaruite (Table 7).

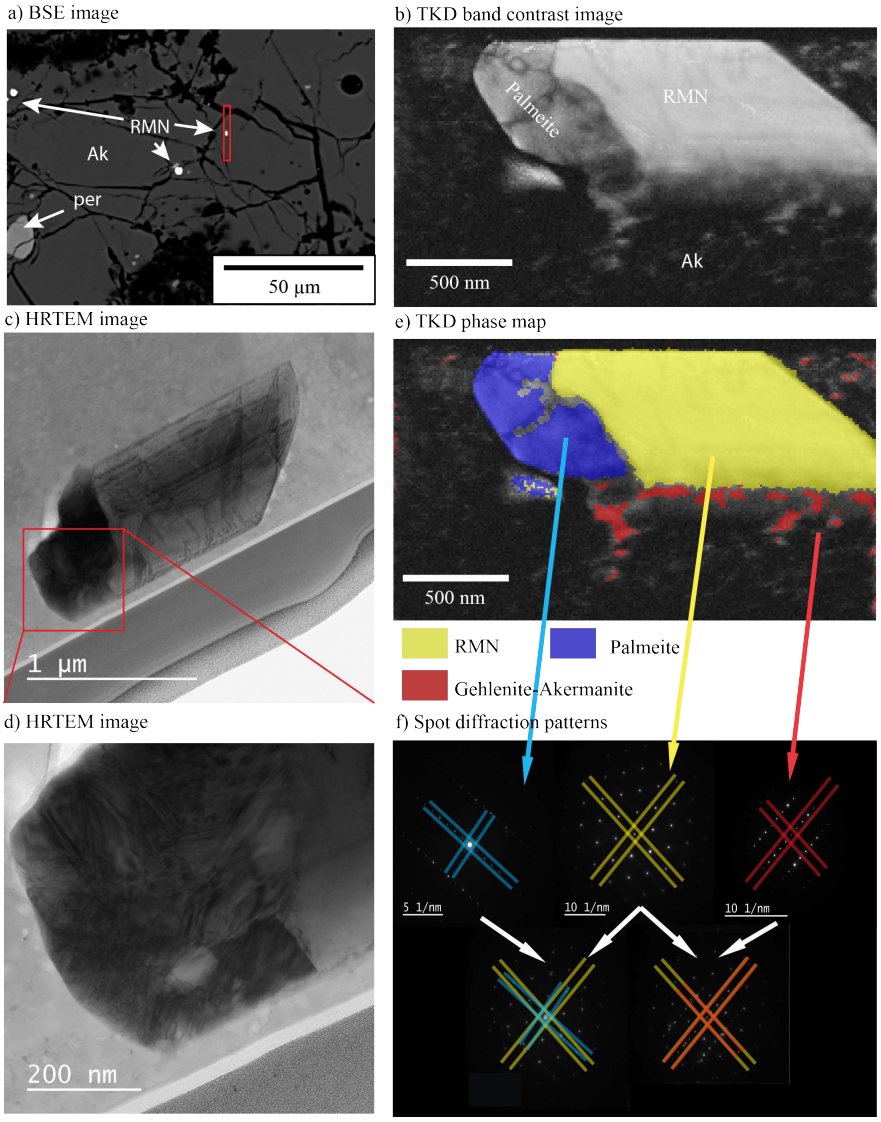

Figure 5: Characteristics of ALH 77307 - region ALH1: TKD analyses from a FIB-produced TEM lamellae of an RMN bearing åkermanite-gehlenite crystal within a Type B-like CAI. a) A BSE image of the RMN *in situ*, prior to FIB extraction, hosted within a Type B-like CAI. Associated minerals are åkermanite-gehlenite (Ak) and perovskite (per), b) TKD band contrast image of the RMN and associated new mineral phase. The labels indicate where EDS spectra from TKD and TEM were taken in Table 5, c) TEM image of the RMN and associated new mineral phase indicating the RMN has several dislocation planes, d) TEM zoomed image of the new mineral phase indicating the phase is heavily dislocated, exhibiting oriented bladed crystal morphologies, e) TKD phase map indicating a euhedral RMN (yellow), its associated new mineral phase (blue), and the åkermanite-gehlenite host (red). The RMN is observed to be euhedral and the new mineral phase adopts a pseudomorph texture with the RMN, f) TEM spot diffraction patterns taken from each phase. These spot diffraction patterns are overlain which revealed a shared <c> crystal axis between the RMN and the new mineral phase within 6°. The RMN [002] axis is shared with the [201] axis of the åkermanite-gehlenite host.

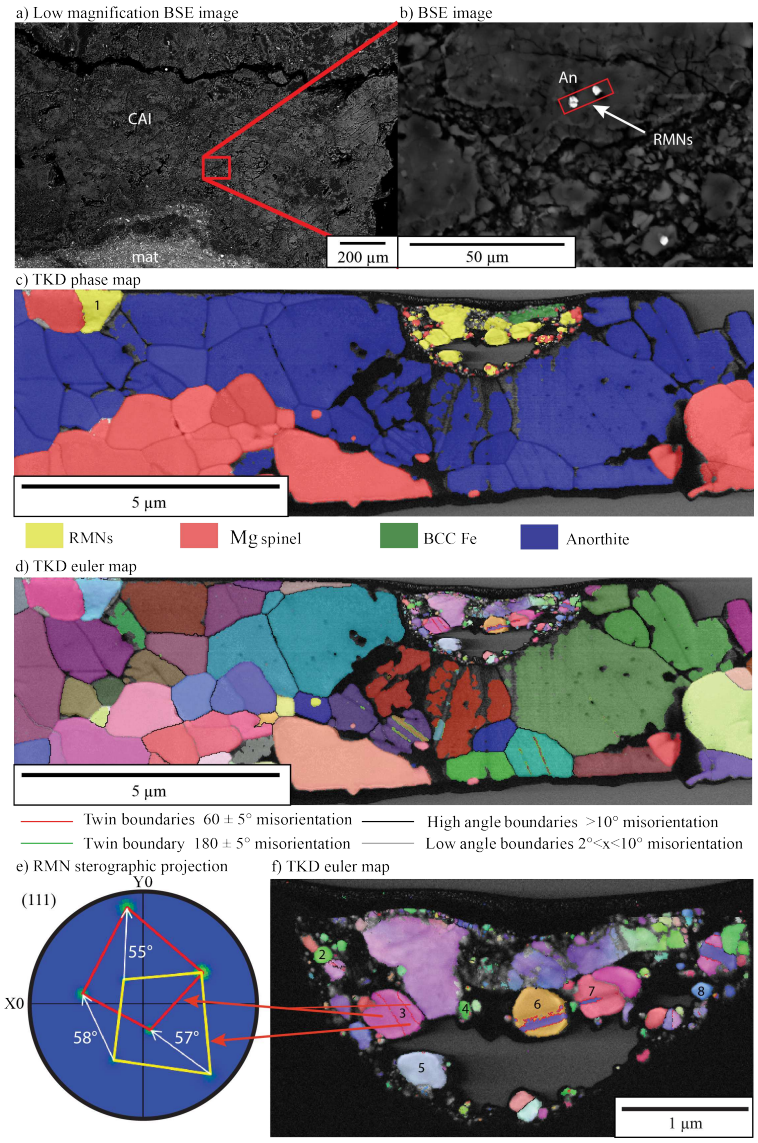

Figure 6: Characteristics of Vigarano - region V1: TKD analyses of a large RMN associated with spinel and a cluster of twinned RMNs in a void. These RMNs are hosted in anorthite contained within the altered mantle of a fluffy-type A CAI. a) A lower magnification BSE image showing the wider context of region V1 within the CAI, b) A BSE image of region V1 prior to sample extraction indicating two RMNs (bright spots). The red rectangle indicates the orientation of the extracted TEM section. The RMNs here are associated with anorthite (An), c) TKD phase map indicating RMNs in yellow. The large RMN to the left of the section is associated with spinel (red). The number indicated the EDS measurement in Table 6. The RMN cluster to the right is within a void encapsulated by anorthite (blue), d) TKD Euler image of the section indicating crystallographic orientations. Grain boundaries are noted by black lines and twin planes are noted in red. The anorthite exhibits twins rotating at 120° around the twin plane, e) Stereographic projection plotting the poles to the crystal face for a twinned RMN indicating a rotation about the [111] axis of 60°, f) A TKD euler image magnified at the right hand side RMN cluster revealing twin planes (red lines) within the RMNs. The numbers indicate the location of EDS measurements detailed in Table 5.

Table 6: EDS measurements taken from region V1. The RMN number corresponds to the numbered regions of Figures 6c and e. b.d. = below detection.

RMN	At%						
	Fe	Ni	Ru	Mo	Os	Ir	Pt
1	40.9	45.0	4.8	b.d.	3.6	b.d.	5.6
2	36.2	9.2	20.5	b.d.	16.0	18.0	b.d.
3	45.8	23.7	13.4	b.d.	9.1	8.1	b.d.
4	33.0	7.8	23.3	b.d.	14.1	21.8	b.d.
5	1.2	35.2	16.0	b.d.	12.0	24.6	11.0
6	38.7	30.3	5.5	b.d.	5.6	8.3	11.7
7	39.2	27.6	8.0	b.d.	8.7	8.8	7.8
8	31.8	9.7	17.4	b.d.	19.2	22.0	b.d.

Table 7: EDS measurements taken from region V2. The label corresponds to the label regions of Figure 7c. b.d. = below detection.

RMN	At%								
	Fe	Ni	Ru	Mo	Os	Ir	Pt	Ca	O
Powellite 1	0.3	b.d.	b.d.	4.5	b.d.	b.d.	b.d.	3.6	91.6
Powellite 2	0.4	b.d.	b.d.	3.9	b.d.	b.d.	b.d.	3.0	92.7
Awaruite	42.3	41.8	8.5	b.d.	b.d.	3.9	3.6	b.d.	b.d.
RMN	45.2	8.4	35.1	b.d.	6.8	3.3	1.2	b.d.	b.d.

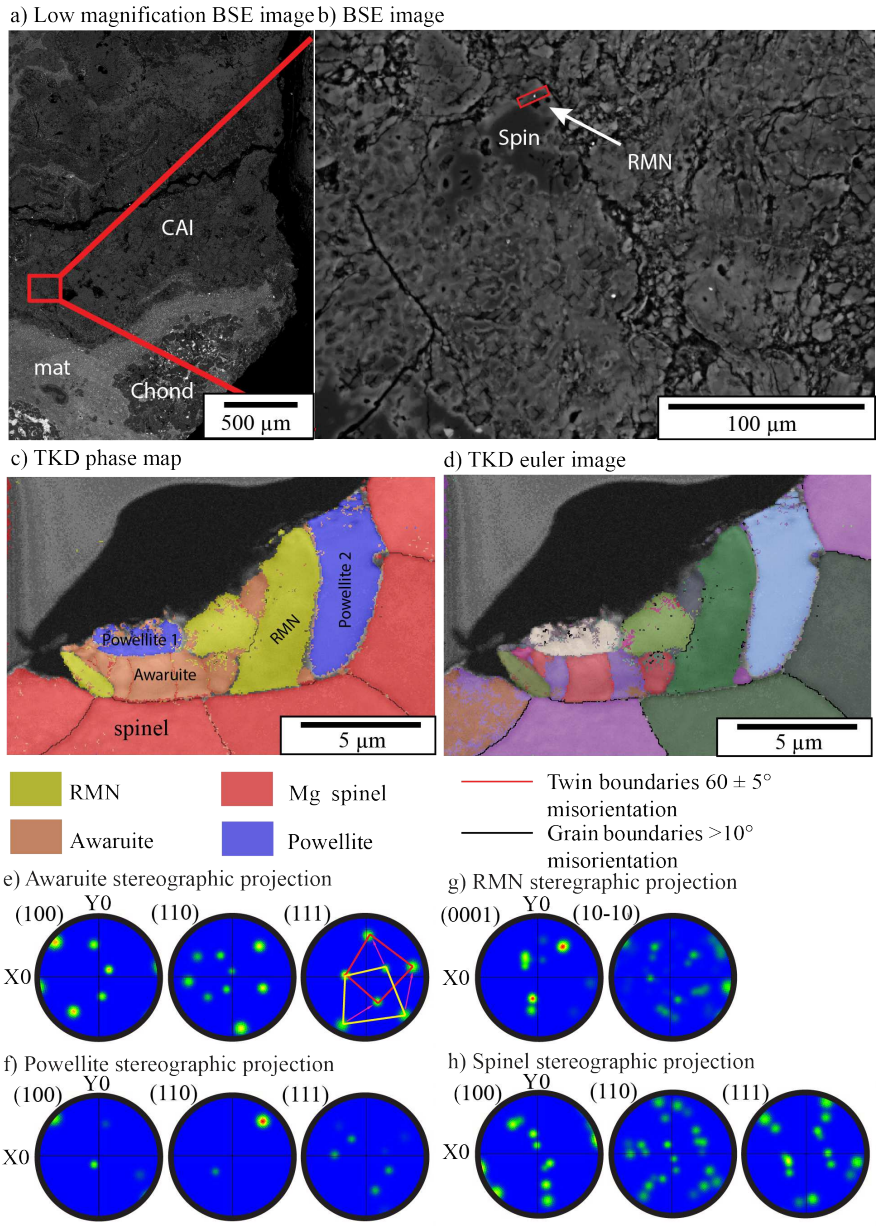

Figure 7: Characteristics of Vigarano - region V2. TKD analyses of RMNs and associated HSE alteration phases. These RMNs are hosted in spinel contained within the altered mantle of a fluffy type A CAI. a) Low magnification BSE image of region V2 in the wider context of the CAI; also showing a neareby matrix region and chondrule (Chond), b) A BSE image of the RMN (bright spot) in context, before extraction. The red rectangle indicates the orientation of the TEM section, the RMN here is associated with spinel (Spin), c) A TKD phase map of the section indicating the RMN (green) powellite (red) and awaruite (blue) assemblage hosted in a spinel (yellow). The labels indicate where EDS spectra were taken in Table 7, d) A TKD euler map indicating crystallographic orientations of all the phases. Twin planes are shown as red lines indicating the awaruite phase is twinned, e) Lower hemisphere stereographic projection of crystallographic orientations of the awaruite, indicating a rotation about the [111] axis of 60°, f) Lower hemisphere stereographic projection of crystallographic orientations of the powellite, g) Lower hemisphere stereographic projection of crystallographic orientations of the two largest RMN grains with a shared pole in the [110] axis, h) Lower hemisphere stereographic projection of crystallographic orientations of the spinel. There is no systematic crystallographic relationship observed between any of the phases.

4. Discussion

Previous studies of RMNs have mostly lacked high resolution *in situ* crystallographic measurements, and instead focussed on the compositional variability between RMNs and mineralogical associations to inform interpretations. This new high resolution data provided by TKD may provide us with the key to accurately interpret the formation history of individual RMNs and any subsequent alteration, based on a synthesis of their petrographic context, morphology, chemistry, and CORs with host phases.

4.1. Allende - region A1

The presence of sulphide hosted RMNs towards the edge of a chondrule requires that these RMNs experienced at least a chondrule formation, and possibly a sulphidation event (Figure 1a).

The subhedral-anhedral morphology of these RMNs (Figure 2), indicates that they grew in a constrained environment where there was competition for space. If this is the case we would expect to see random orientations between RMNs. Another possibility is that the RMNs are the metal remnants of a sulphidised metal nodule. In this case we would expect to see a shared alignment between all the RMNs.

Iron was uniformly distributed across all RMNs in the section. Nickel was also uniform except for one grain which was significantly enriched (Table 2). The HSEs Ir and Pt however, exhibited a variety of compositions, while Mo and W were completely absent and Os was only present in one RMN (Table 2). It is possible that these RMNs formed by the precipitation of dissolved Pt and Ir from a silicate melt (Schwander et al., 2015a,b). This mechanism requires that the HSEs completely dissolve into the melt. The HSEs have extremely high distribution coefficients, $D^{metal/silicate}$, of approximately 10^4 suggesting that most of the HSEs should remain in the metal phase (Grossman, 2010; Borisov & Palme, 1995, 1997). However, because the metal is such a small proportion of the overall material in an inclusion, it may be possible to dissolve supra-chondritic abundances of HSE in a silicate melt under nebular conditions (Schwander et al., 2015b; Cottrell & Walker, 2004, 2006). If precipitation is producing RMNs and all the HSEs were dissolved and subsequently precipitated during quenching, the composition of the RMNs would become homogenised with increased time in the molten state. Therefore, the composition of the RMNs within the quenched product would either be identical, or exhibit systematic variabilities in the chemistry of RMNs from rim to core based on the variable rate of diffusion between HSEs. The only way to produce heterogeneous RMN compositions by precipitation is to maintain original inherited heterogeneities in the chondrule precursor material by short lived heating events, which would not allow HSEs to homogenise throughout the melt phase. This means heterogeneous RMNs will preserve their primordial chemistry. Therefore heterogeneous RMN compositions provide evidence for primordial chemical signatures, and RMNs with more uniform CV elemental ratios are evidence of increased time in the molten state. In this region, the RMNs show a factor of 10 deviation from bulk CV over a distance of 10 µm, implying that if the RMNs are produced by precipitation, the chondrule cannot have remained molten for an extended period of time, and these RMNs preserve their primordial elemental abundance. The unique HSE composition of each RMN in this case is more readily explained if

these RMNs were stable metal inclusions that did not dissolve. The HSE composition of these inclusions is related to the primordial composition of the RMN - their composition when they were incorporated into the chondrule precursor. Stable metal inclusions have been demonstrated by Yokoyama et al. (2009) and Médard et al. (2015). Earlier work by Borisov & Palme (1997) and Ertel et al. (1999, 2006) supports a stable origin of compositionally heterogeneous inclusions.

The absence of Mo, W and Os can be readily explained by heating at high oxygen fugacities during the chondrule formation event (Jones & Scott, 1996; Palme et al., 1998). The uniform abundance of Fe is likely to be produced during the sulphidation event by equilibration of the Fe in the RMN with that of the surrounding sulphide. The enrichment of Pt is unlikely to be as excessive as the EDS data suggests due to the contribution of Pt from the fluorescence of the Pt protective layer emplaced during the FIB process. EDS measurements from EBSD indicate Ir and Pt relative abundances were highly variable but with much lower Pt than observed in TKD (Table 1). This generates Ir/Pt ratios between 5.4-0.3, inconsistent with a bulk CV Ir/Pt ratio of 0.6 (Wasson & Kallemeyn, 1988). Furthermore, current condensation models do not predict such low Ir/Pt ratios.

The RMNs in this section are all aligned and share a [100] axis with forsterite (Figures 1 & 2). Possible mechanisms that could produce this are: a) RMNs forming as interconnected 3D 'worm-like' structures, b) Alignment of minerals with high magnetic susceptibilities under the influence of a magnetic field, c) Alignment during crystallisation due to a minimisation of interfacial energy, d) Original alignment of Fe-Ni metal nodules that have been replaced by sulphide preserving only HSE-rich alloys. There is no possibility of producing the observed alignment by compaction.

The possibility that these RMNs are not discrete grains but rather part of a single grain with a complex 3D structure is unlikely. Observations during FIB preparation discount this hypothesis, revealing that these RMNs are in fact isolated grains. Furthermore if the RMN consisted of one large tubular crystal we would expect the chemical composition of each RMN to be identical, which is not the case.

Studies such as Dai et al. (2001), Inomata et al. (1988), Rellinghaus et al. (2003) and Luo & Sellmyer (1999) have shown that some Fe-Pt alloys can exhibit magnetic properties from paramagnetic to high uniaxial magnetocrystalline anisotropy to superparamegnetic. These properties are strongly dependent on the composition and structure of the phase. Some HSE bearing phases have been separated from samples magnetically (Horan et al., 2009). The possibility that RMNs could be oriented in a magnetic field by suspended RMNs rotating in a rapidly solidifying melt concordant with the magnetic field should be considered. It would require RMNs to have a high magnetic susceptibility with a high magnetocrystalline anisotropy. Magnetic susceptibility of PtIr alloys is approximately $1\text{x}10^{-6}$ m^3/kg (Budworth et al., 1960), much lower than a mineral such as magnetite which has a mass magnetic susceptibility of approximately $2 - 11\text{x}10^{-4}$ m^3/kg (Hunt et al., 1995). Magnetite requires exposure to a strong stable field (e.g., a bar magnet) to induce a crystallographic alignment. Such a field is unlikely to occur within the solar nebula. Even if such a field existed RMNs suspended in a fluid would be expected to grow unimpeded and we should therefore observe

euhedral RMNs, which is not the case.

The crystallographic relationship observed between the forsterite grains and RMNs by way of a shared [100] axis suggests the orientation may be produced during crystallisation of forsterite incorporating RMNs by way of minimising interfacial energy (Frondel, 1940), see also reaction fabric (Lauder, 1961)) as it envelops the RMNs. This readily explains the shared alignment of the RMNs with each other as well as with the forsterite. However, this orientation relationship must be preserved during sulphidation and the formation of the pentlandite. As not all RMNs are in direct contact with the forsterite it is hard to imagine a situation in which these isolated RMNs could also obtain this preferred alignment as pentlandite is not thought to directly replace forsterite. However, sulphides are expected to form by sulphidation of metals (Lauretta et al., 1996). In this scenario, a metal nodule was incorporated into the chondrule. When the forsterite crystallised it adopted the orientation that minimised the interafcial energy. The chondrule was then exposed to a sulphur rich gas which sulphidised the metal nodule. The question is then raised are these RMNs residual nucleation cores (Petaev et al., 2003) or the result of the diffusion of HSEs away from the reaction front. If the RMNs were residual nucleation cores we would expect them to have a euhedral structure and non-uniform orientation, which is not the case. Therefore, it is probable that these RMNs were the product of migrating HSE elements which are more compatible with the metal phase (Ir, Pt). The heterogeneous chemistry is generated by either heterogeneous distribution of HSEs in the nodule, or heterogeneities in local mineral chemistry - proximity to forsterite or proximity to troillite etc, or variable sizes of the 'catchment area' from which the HSEs were delivered to the RMN.

In summary, the most likely sequence of events that occurred to produce the RMNs in Allende - region A1 is a metal nodule containing HSEs condensed and was incorporated into a chondrule precursor. This material was heated, melting the forsterite but not the metal nodule, and formed the chondrule. Tungsten, Mo and Os are likely to have been removed due to the high oxygen fugacities associated with chondrule formation (Jones & Scott, 1996; Palme et al., 1998). On cooling the forsterite crystallised around the metal nodule minimising the interfacial energy, and producing the shared crystallographic alignment. The chondrule was then exposed to a sulphur-rich gas which sulphidised the metal grain. HSEs incompatible with the sulphide phase migrate into the receding metal phase eventually forming small anhedral RMNs with variable HSE compositions.

4.2. Allende - region A2

The RMNs here are hosted in a forsterite grain within a CAI. The CAI has undergone some recrystallisation due to annealing which caused a change in the grain boundary network from elevated temperatures without differential stress. This produced the equigranular texture of the surrounding spinel with 120° grain boundary intersections.

The RMNs in this section are separated into two morphologies: a large RMN associated with molybdenite and smaller spherical RMNs hosted within the forsterite. The spherical morphology of these RMNs is indicative of the formation of two immiscible fluids, in this case a silicate and a metal phase. The spherical

morphology was maintained during crystallisation by the surface tension between the fluids, which prevented the RMN adopting its preferred cubic habit. If the RMN was miscible with the silicate melt we would expect normal igneous textures to form, for example if the RMN crystallises first euhedral RMNs form, and subhedral-anhedral RMNs form if the RMN crystallises simultaneously with another phase. The presence of spherical RMNs coupled with a lack of any COR between RMNs, or with the host forsterite crystal, requires that the whole forsterite-RMN assemblage was melted under environmental conditions that promoted the separation of metal and silicate melts. The melting point of RMN alloys is not well constrained, although the melting point of pure element phases such as Os under normal atmospheric conditions is known to be very high (3127 °C) (Griffith, 2009). This is much higher than that of forsterite. We would expect that the melting point of a mixed HSE alloy to be lower than the pure phase and the RMN melting point would decrease under vacuum. However, the triple point of forsterite under nebular conditions is approximately 1890 °C (Nagahara et al., 1994) which is lower than the melting point expected of RMNs. This presents a problem as a significant difference between the vaporisation temperature of forsterite and the estimated melting temperature of RMNs means the two phases are unlikely to coexist in a melt. A further possibility is that the forsterite inclusion was melted within the CAI. This would require that the surrounding spinel phase did not melt, meaning that the temperature did not exceed 2135 °C (Ping et al., 2001). This is within a realistic range for the production of two immiscible fluids of metal and silicate whilst also isolating the inclusion and maintaining a closed system. Spherical RMNs have been observed by Schwander et al. (2015b). These authors concluded that these RMNs were derived from the precipitation dissolved HSEs into metal grains from a CAI like liquid. They suggested the resulting precipitate would produce RMNs with spherical morphologies though a minimisation of the surface energy at the RMN grain boundary and the surrounding liquid. In this scenario only the forsterite is required to melt, and the HSEs will dissolve into the melt over time. This scenario therefore solves the temperature dichotomy between the melting points of the two phases. Upon cooling, diffusion of HSE metals was not fast enough or cooling was too rapid to allow the precipitation of a single RMN, and instead precipitated several smaller RMNs. If this was the case we would expect the RMN compositions in this region to be similar.

The RMNs in this section have identical compositions indicating that these RMNs were homogenised. The RMNs are devoid of Mo with the exception of the two large RMN crystals intergrown with the molybdenite phase. This is likely to be due to fluorescence from the nearby molybdenite, which is likely contaminating the spectra. We cannot rule out the incomplete segregation of Mo from the metal to sulphide phase. However, the molybdenite comprises approximately 1/3 of the area of the large RMN. Therefore, the abundance of Mo within the molybdenite phase could have been reasonably acquired from the RMN phases assuming the RMN initially contained approximately chondritic abundances of Mo. The RMNs are also devoid of Ni. Osmium and Ir are within 20% of their chondritic ratios, whereas Ru exhibits an enrichment of around 40-60% with a Ru/Os ratio between 1.5 and 2. This is higher than the maximum Ru/Os predicted for condensation derived RMNs. Therefore the Ru enrichment is likely due to the initial incorporation of an Ru-enriched primordial

RMN.

The two larger RMNs have an identical COR with the associated molybdenite. This, as well as the 'interfingering' of the molybdenite with the large RMN is consistent with a reaction texture caused by the separation of the two phases. The large RMNs and the molybdenite were significantly more deformed than the small RMNs and the forsterite. This means it is likely that these phases were present before the event that formed the spherical RMNs. If we assume that the smaller spherical RMNs are indeed produced by precipitation of dissolved HSEs, the source of these HSEs could be the larger RMN. The size of the forsterite grain compared with the RMN, combined with the large partition coefficient for the HSEs, which will prevent HSEs dissolving into the silicate melt, and the preserved dislocations in the RMN and molybdenite mean it is unlikely that the whole RMN dissolved. However, sufficient HSEs did dissolve to form small uniform spherical RMNs on quenching of the forsterite. The melting event, though insufficient to melt the RMN, could plausibly provide the energy required to generate the reaction texture between the molybdenite and the large RMN.

As all other HSEs have approximately CI relative abundance ratios we can calculate if any Mo has been added or removed. A first order approximation for the abundance of Mo if it is distributed evenly amongst the RMNs reveals an approximate CI relative abundance. This suggests a closed system within the inclusion: Mo and S must have been present initially within the inclusion.

In summary the most likely sequence of events experienced by this section is that an RMN-bearing forsterite grain was heated, which melted the forsterite and dissolved some of the HSE elements into the silicate melt, homogenising their chemistry. The residual RMN also separated into a molybdenite phase and a metal phase which preserved primary dislocations and produced the reaction texture observed. Upon cooling, the dissolved HSEs precipitated into spherical RMN droplets forming an immiscible metal-silicate melt. The RMNs were chemically homogenised as the HSEs were evenly distributed throughout the forsterite melt. Rapid cooling then precipitated RMNs faster than the diffusion pathway isolating small metal droplets prior to forsterite crystallisation. The surface tension between the silicate and metal melts then caused the RMNs to form a spherical morphology on cooling.

4.3. Allende - region A3

This RMN was hosted in the core of a forsterite inclusion surrounded by augite in a CAI. The augite had a crystalline equigranular texture implying that the CAI was recrystallised due to annealing at elevated temperatures in the absence of a differential stress field.

The RMN shared a [110] axis with the forsterite. This is similar to the observed COR between RMNs and forsterite in region A1 where the [100] was shared. Here the RMN was situated in the core of the forsterite inclusion. However, the RMN may still have formed due to the minimisation of interfacial energy between it and the forsterite, as was the case for the original metal nodule in region A1. In this scenario, it is possible that the RMN provided the nucleation site of the forsterite, as it is situated in the core of the inclusion.

There are two types of nucleation: homogeneous and heterogeneous. Homogeneous nucleation occurs when the crystal nucleates from a newly formed embryo of similar material, whereas, heterogeneous nucleation occurs when a crystal nucleates off a pre-existing nuclei or pre-existing mineral (Herlach, 1994). Homogeneous nucleation occurs at lower temperatures and slower cooling rates as the embryos require time to form. Conversely, heterogeneous nucleation occurs at initially high temperatures followed by subsequent rapid cooling (Herlach, 1994). Homegeneous nucleation would not generate a crystallographic relationship between the forsterite and the RMN. Therefore, it is more likely that the forsterite nucleated heterogeneously around an RMN. This scenario requires the pressure temperature conditions to be above the formation temperature of forsterite nuclei embryos, and rapid cooling.

4.4. ALH 77307 - region ALH1

The RMN in this section is hosted within a type B-like CAI and is associated with a potential new mineral phase which adopted a pseudomorph texture with the RMN. The RMN has a euhedral morphology indicating the RMN must have grown in an initially unconstrained environment.

The new mineral phase was likely to be a secondary phase formed by alteration of the RMN, separating Mo and W into the new phase due to their increased mobility during alteration events (Palme et al., 1998). The pseudmorph texture indicated that the secondary alteration must have occurred whilst the RMN was within the CAI, a confined space. The process that caused this phase separation must have occurred at temperatures lower than the melting point of the åkermanite-gehlenite host ($1410 - 1510$ °C (Mendybaev et al., 2006)). If this was not the case the new mineral phase would have been able to grow unconstrained, and would not exhibit the observed deformation features, or conform to the original RMN grain boundary. There are two possible alteration sites: alteration on the parent body, or alteration in the nebula. ALH 77307 is one of the most primitive meteorites in the collection, with a maximum parent body temperature of 203 °C (Cody et al., 2008).

The observed textures within the new mineral phase exhibit a high dislocation density indicating the mineral may have formed rapidly. However, the TKD data indicate these dislocations have significant orientation changes between grains of the new mineral phase while maintaining a COR with the RMN. This suggests either crystal plastic deformation or rapid formation occurred. Crystal plastic deformation requires an induced stress field, which is unlikely and therefore it is probable that this new mineral phase formed rapidly. To maintain the pseudomorph texture the temperature cannot have exceeded the åkermanite-gehlenite melting point and therefore the RMN itself cannot have melted. The new phase must have exsolved and replaced the RMN by solid state recrystallisation. We suggest this new phase formed during a transient heating event in the protoplanetary disk, prior to the incorporation of the CAI into the parent body. The temperatures required to produce this new phase are unconstrained so we cannot rule out parent body alteration as a formation mechanism based on temperature. Rapid formation of the new phase is inconsistent with regional parent body alteration.

The RMN shares a minor axis with the åkermanite-gehlenite host. This COR with the åkermanite-gehlenite mineral strongly implies that the åkermanite-gehlenite crystal nucleated around the RMN. This is interpreted along a similar line of reasoning to region A3, which also exhibits heterogeneous nucleation of åkermanite-gehlenite around a pre-existing RMN. The RMN also shares a major axis with the new phase to within 6 °. This supports the notion that the new phase exsolved from the RMN and formed rapidly, producing an imperfect COR.

These observations indicate that this CAI must have experienced at least two heating events: one to produce the type-B CAI texture which would have melted the inclusion at temperatures above 1510 °C (Mendybaev et al., 2006), and a second sequence of rapid cooling which produced heterogeneous nucleation of åkermanite-gehlenite around the RMN. This was followed by a second transient heating event below 1410 °C (Mendybaev et al., 2006) that exsolved the new phase from the RMN and produced the pseudomorph texture and the observed crystallographic alignments, as well as annealing the CAI.

4.5. Vigarano - region V1 and V2

The CAI bearing the V1 and V2 regions has a zoned texture with a relatively unaltered core,. There is potentially re-heated material surrounding the core, and Wark Lovering rims around the edge of the CAI. The region is interpreted as 're-heated' due to the presence of annealing textures such as 180° mirror twins within the anorthite (Figure 6) and 120° grain-boundary-intersection spinel grains (Figure 7). The RMNs were extracted from this re-heated portion of the CAI, and are hosted within an anorthite grain (Region V1) and a spinel grain (Region V2).

The RMNs in V1 had two distinct morphologies: an anhedral RMN associated with spinel, and several euhedral twinned RMNs with straight grain boundaries (Figure 6). The euhedral RMNs likely formed in an unconstrained environment in the presence of a fluid or gas. Their accumulation in a void space indicates that they may have originally been free floating in the nebula gas. The RMN associated with the spinel is anhedral, indicating it formed in a confined space. The region V2 contains a complex HSE-rich inclusion and is unlike any previously described RMN. The RMN has separated into three phases: a Mo-rich powellite, a Ni-rich twinned awaruite and an Os, Ru-enriched RMN. It is unclear whether this region was once a single RMN that has since separated or was initially incorporated as an agglomeration of phases (Figure 7).

The chemistry of each RMN in V1 is unique, and none have chondritic relative elemental ratios even though these grains are hosted within the same CAI, and in some places are situated adjacent to each other. However, an 'average' RMN derived from the mean HSE abundance of these RMNs is much more consistent with chondritic elemental ratios. None contain detectable Mo. This indicates that with the exception of Mo and W, HSEs in RMNs are resistant to remobilisation. There is no transfer or re-equilibration of HSEs, even between RMNs separated by only a few nanometres. The HSE aggregate in V2 contains two metal phases: awaruite and the RMN, which exhibit a complementary depletion or enrichment in Ru and an enrichment or depletion in Ni, respectively. The powellite is the only phase present to contain Mo. The redox state of Mo implies the event that mobilised the Mo was oxidising and likely occurred within the CAI which provided

the Ca component. This containment in the CAI inhibited the escape of Mo. All of the phases exhibit large deviations from chondritic relative abundances.

The RMN associated with spinel in V1 likely formed together as a single inclusion that was subsequently incorporated into the CAI. It is possible that the RMN and spinel formed a metal-silicate immiscible fluid as there is a slight curvature of the grain boundary towards the bottom of the inclusion. This could be interpreted as the meniscus between two immiscible fluids, coupled with the observation that the inclusion itself is spherical. Therefore the most likely interpretation is that an RMN was incorporated into a spinel precursor material. This material was then completely melted forming two immiscible fluids which subsequently cooled together, preserving the meniscus, and was then incorporated into the CAI (Figure 6). The composition of this RMN is very close to chondritic relative abundance of the remaining HSEs. This supports the idea that the RMN formed an immiscible fluid with the silicate, or potentially precipitated from the silicate melt after the HSE elements had diffused (Schwander et al., 2015b) and homogenised throughout the melt. In this case, the cooling rate was sufficiently slow to permit the formation of a single large homogeneous RMN.

The crystal twins observed within RMNs in Vigarano in both the euhedral RMNs in V1 (Figure 6) and the awaruite in V2 (Figure 7) have not previously been reported in RMNs despite numerous and detailed microscopy (Sylvester et al., 1990; Schwander et al., 2015b; Wark & Lovering, 1976) and TEM studies (Harries et al., 2012; Croat et al., 2013). This demonstrates the value of TKD and its ability to map the crystallography and chemistry of a lamella rapidly, in comparison to established techniques such as TEM. Twinning can be produced via a number of different mechanisms, such as growth, annealing and deformation (Cahn, 1954). The Vigarano meteorite has undergone very little processing in terms of deformation and shock (Scott et al., 1992). Therefore, it is reasonable to assume that these twins are not derived from shock related processes within the parent body.

This leaves two possibilities: growth twins and annealing twins. If the observed twins were growth twins formed from nucleation these would be observed as simple penetration twins. This would result in clear crystal faces with changes in the morphology of the RMN which are coincident with the twin boundary. This is not observed within the sample as the crystal faces are well formed and continuous across the twin boundary. We would also expect this to be a much more common observation in RMNs if they formed growth twins.

Annealing twins form at high temperatures with relatively little stress. In fcc crystals they classically form along the [111] axis with a 60° misorientation (Brandon, 1966), which is consistent with the observed RMN twins in Vigarano (Figure 6). This implies that the twinning observed is probably formed by annealing. TEM experiments by Dai et al. (2001) observed annealing twin formation in FePt nanoparticles. This study indicated that while heating under vacuum for one hour, annealing twins began to form at 450 °C, and were completely annealed by 530 °C. The nanoparticles studied coalesced into larger grains at $600 - 700$ °C. The RMNs observed in Vigarano, however, have not coalesced. The specific grains in the aforementioned study are compositionally different to RMNs observed in our research, so only limited caparisons can be

made. Nevertheless, it does give an approximate temperature at which annealing twins might start to form in RMNs.

These annealing twins could form either as a result of parent body alteration, or pre-accretion in the nebular either as free floating RMNs or subsequent to the RMNs incorporation into the CAI.

The CAI did contain nephaline and sodalite which are evidence for parent body alteration (Krot et al., 1997). Although a low stress environment is consistent with the shock history of the Vigarano parent body, a high temperature environment clearly is not. The highest estimates place the maximum parent body temperatures experienced by Vigarano at 415 °C (Cody et al., 2008), and most estimates for Vigarano peak temperatures are much lower than this (<330 °C) (e.g. Bonal et al. (2006, 2007)); below the minimum temperature required to anneal the RMNs. Therefore, it is unlikely that the annealing twins formed on the Vigarano parent body, suggesting pre-accretion annealing of RMNs occurred. This leaves two possibilities: either the annealing twins formed in the nebula prior to incorporation into the CAI or post incorporation into the CAI.

Temperatures capable of annealing RMNs could have been experienced in the nebula environment either prior to or post-incorporation into the host; a 'fluffy' type-A CAI. However, as CAIs are thought to form at high temperatures, the annealing textures would likely be overprinted during CAI formation.

The texture of the CAI indicates it has undergone a transient heating event post formation, however, this texture is only observed in the mantle of the CAI with a relatively pristine core. The fact that the whole CAI does not show this temperature-induced annealing indicates that the event was short lived. Rapid growth of annealing twins is supported by the observations of Dai et al. (2001). This constrains possible mechanisms for heating to short lived events. Otherwise the core of the CAI would have completely equilibrated and exhibited similar heating signatures to the rest of the inclusion. Furthermore, the HSE agglomerate in V2 is contained by the surrounding spinel, as it still retains a Mo-rich phase as well as anneling twins in the awaruite. This supports the argument that the RMN was contained within the CAI during the phase separation that provides the Ca for the powellite mineral. Therefore it is likely that the annealing twins formed once the RMNs were incorporated into the CAI. This implies that the RMNs did not experience temperatures above the melting point of anorthite at $\sim$ 1550 °C (Hariya & Kennedy, 1968) (although lower melting points have been reported of 1293 °C (Komatsu et al., 2009)) or the melting point of spinel 2350 °C (Ping et al., 2001), as the textures of the CAI are inconsistent with a melting event. Thus we can constrain a maximum temperature experienced by the clast during the event that reheated the CAI to form the annealed altered mantle.

Annealing twins could be used to define a temperature range for heating events, as the onset of annealing occurs at a specific temperature and complete recrystallisaiton occurs at a higher temperature. This allows annealing textures to be used as a low resolution thermometers for pre-accretion heating events. The host mineral phase in the CAI is used to approximate a maximum formational temperature as shown above, and annealing experiments on FePt alloys by Dai et al. (2001) were used to approximate a minimum temperature.

Combining these observations we interpret that the thermal history of this CAI in Vigarano experienced a short lived high temperature event pre-accretion between $\sim 500 - 1200$ °C.

4.6. Summary

RMNs are a complicated mineral phase in meteorites. It is apparent that each individual RMN preserves a unique history of Solar System events and possibly even pre-solar events.

The morphology of RMNs may indicate the processes and environment the RMN formed in, i.e., euhedral RMNs are naturally expected to form in unconstrained environments such as growth in a fluid or gas phase. If this growth is impeded or the RMN is subsequently altered we would expect to observe anhedral-subhedral RMNs. Spherical RMNs have been observed and interpreted as precipitatates from a silicate melt forming an immiscible fluid during solidification, as suggested by Schwander et al. (2015b).

The analyses of RMNs using TKD has revealed several crystallographic textures that had not been documented previously. These observations provide evidence for, and constraints on, several Solar System processes. CORs between RMNs and their host and petrological data can be used to determine whether the RMNs were rotated due to a minimisation of surface energy. This is likely for RMNs which occur along grain boundaries, or if the RMN acted as a heterogeneous nucleation site for the host phase during crystallisation. Here, they would likely occur in the centre of a crystal. The presence of annealing twins, indicated RMNs can preserve evidence of low temperature heating events and can therefore act as a coarse thermometer indicating, in this case, the host CAI experienced heating, pre-accretion to $\sim 500 - 1200$ °C. The context of the RMN in relation to its host phase and inclusion can also indicate when and where the RMN was altered. The thermodynamic properties of the RMN and its surrounding phases can refine interpretations for their formation history. For example, annealing twins must have occurred in the nebula, as the Vigarano parent body did not experience the required temperatures to produce this texture.

The relative chemical abundances of HSEs in RMNs are highly variable with the exception of the small spherical RMNs in A2 which have uniform chemistry with near chondritic relative elemental abundances. RMNs in A2 are therefore interpreted to have precipitated as suggested by Schwander et al. (2015b) and Schwander et al. (2015a), due to their homogeneous chemistry. However, these RMNs are also situated next to a RMN which appears to preserve dislocations and a reaction texture, signifying it formed before the melting event. RMNs in A1 appear to be able to form by migration of HSEs during sulphidation of metal nodules. In all other RMNs in this study, including highly altered RMNs, we still observe unique non-chondritic abundances of at least two HSEs. HSE elements Os, Ir, Pt and Ru are observed to be largely unaffected by most asteroidal processes. Os can be mobilised in transient heating events at high oxygen fugacities. Tungsten and Mo are mobilised by low levels of alteration in either a high oxygen fugacity environment or in the presence of sulphur. Isolated RMN-bearing inclusions can preserve Mo and W where they are encapsulated within an impermeable host. The immobility of most HSEs is evident even in RMNs in the same inclusion, same host mineral and even in some separated by a few nanometres of void space. This suggests that RMNs are highly resistant to re-equilibration, and individual RMNs can be approximated

to a closed system during the majority of Solar System processes with regard to these elements. Therefore the refractory component of RMNs may preserve a primary or even pre-solar signature.

Combining these observations provides evidence that supports the suggestion of Daly et al. (in review); RMNs that have not been homogenised during melting, preserve a primordial signature that is inconsistent with condensation and is likely to have originated as part of an inherently diverse population of RMNs distributed throughout the Giant Molecular Cloud. Isotopic analyses of individual RMNs would provide a clear answer to this hypothesis.

5. Conclusions

TKD and other high resolution *in situ* analyses are integral to the interpretation of RMNs, enabling us to evaluate the sequence of events that may have affected RMN chemistry and relations to host inclusions since the formation of the RMN. Every section analysed in this study could not be fully interpreted without the incorporation of every facet of information provided by TKD analyses. The relationships between RMN chemistry, morphology, CORs and mineral associations observed in this study combine to form a powerful dataset that can begin to build a framework from which RMN formation and alteration can be determined. Previous work on RMNs showed that they exhibit highly heterogeneous chemical compositions, inconsistent with a single formation model (Daly et al., in review). TKD of RMNs reveals a suite of crystallographic features such as twinning, CORs and randomly oriented spherical nano-RMNs interpreted here as annealing twins, reaction textures, nucleation centres and fluid immiscibility/precipitation textures. This indicates that RMNs experienced a diversity of formation histories even between RMNs within the same meteorite, inclusion, and even separated by a few nanometres. In cases where the RMN has experienced extensive alteration we still observe 'unique' chemical heterogeneities between most RMNs. The variety of crystallographic textures observed indicate each individual RMN has a complex and unique formation history. These observations are consistent with the suggestion of Daly et al. (in review), that some RMNs have survived Solar System formation and preserve an inherited heterogeneity from the Giant Molecular Cloud.

6. Acknowledgements

This work was funded by the Australian Research Council via their Australian Laureate Fellowship program. This research was undertaken on the XFM beamline at the Australian Synchrotron, Victoria, Australia. The authors acknowledge the facilities, and the scientific and technical assistance, of the Australian Microscopy & Microanalysis Research Facility at the Australian Centre for Microscopy and Microanalysis, the University of Sydney and the Centre for Microscopy, Characterisation and Analysis, University of Western Australia. The authors would also like to thank the rest of the Desert Fireball Network research group as well as, Mr Mark Daly, and Ms Jennifer Porter for their assistance.

References

Berg, T., Maul, J., Schönhense, G., Marosits, E., Hoppe, P., Ott, U., & Palme, H. (2009). Direct evidence for condensation in the early solar system and implications for nebular cooling rates. *The Astrophysical Journal Letters*, *702*, L172–L176.

Bischoff, A., & Palme, H. (1987). Composition and mineralogy of refractory-metal-rich assemblages from a Ca, Al-rich inclusion in the Allende meteorite. *Geochimica et Cosmochimica Acta*, *51*, 2733–2748.

Blander, M., Fuchs, L., Horowitz, C., & Land, R. (1980). Primordial refractory metal particles in the Allende meteorite. *Geochimica et Cosmochimica Acta*, *44*, 217–223.

Blum, J. D., Wasserburg, G. J., Hutcheon, I. D., Beckett, J. R., & Stolper, E. M. (1988). 'Domestic' origin of opaque assemblages in refractory inclusions in meteorites. *Nature*, *331*, 405–409.

Bonal, L., Bourot-Denise, M., Quirico, E., Montagnac, G., & Lewin, E. (2007). Organic matter and metamorphic history of CO chondrites. *Geochimica et Cosmochimica Acta*, *71*, 1605–1623.

Bonal, L., Quirico, E., Bourot-Denise, M., & Montagnac, G. (2006). Determination of the petrologic type of CV3 chondrites by Raman spectroscopy of included organic matter. *Geochimica et Cosmochimica Acta*, *70*, 1849–1863.

Borisov, A., & Palme, H. (1995). The solubility of iridium in silicate melts: new data from experiments with Ir 10 Pt 90 alloys. *Geochimica et Cosmochimica Acta*, *59*, 481–485.

Borisov, A., & Palme, H. (1997). Experimental determination of the solubility of platinum in silicate melts. *Geochimica et Cosmochimica Acta*, *61*, 4349–4357.

Brandon, D. (1966). The structure of high-angle grain boundaries. *Acta metallurgica*, *14*, 1479–1484.

Budworth, D., Hoare, F., & Preston, J. (1960). The thermal and magnetic properties of some transition element alloys. *Proceedings of the Royal Society of London A: Mathematical, Physical and Engineering Sciences*, *257*, 250–262.

Cahn, R. (1954). Twinned crystals. *Advances in Physics*, *3*, 363–445.

Campbell, A. J., Humayun, M., Meibom, A., Krot, A. N., & Keil, K. (2001). Origin of zoned metal grains in the QUE94411 chondrite. *Geochimica et Cosmochimica Acta*, *65*, 163–180.

Cody, G., Alexander, C. O., Yabuta, H., Kilcoyne, A., Araki, T., Ade, H., Dera, P., Fogel, M., Militzer, B., & Mysen, B. (2008). Organic thermometry for chondritic parent bodies. *Earth and Planetary Science Letters*, *272*, 446–455.

Cottrell, E., & Walker, D. (2004). Ultra-High Temperature Effects in Earth's Magma Ocean: Pt and W Partitioning. *Workshop on Oxygen in the Terrestrial Planets*, *Abstract #3046*.

Cottrell, E., & Walker, D. (2006). Constraints on core formation from Pt partitioning in mafic silicate liquids at high temperatures. *Geochimica et Cosmochimica Acta*, *70*, 1565–1580.

Croat, T., Berg, T., Bernatowicz, T., Groopman, E., & Jadhav, M. (2013). Refractory metal nuggets within presolar graphite: First condensates from a circumstellar environment. *Meteoritics & Planetary Science*, *48*, 686–699.

Dai, Z., Sun, S., & Wang, Z. (2001). Phase transformation, coalescence, and twinning of monodisperse FePt nanocrystals. *Nano Letters*, *1*, 443–447.

Daly, L., Bland, P., Dyl, K., Forman, L., Evans, K., Trimby, P., Moody, S., Limei, Y., Liu, H., Ringer, S., Ryan, C., & Saunders, M. (in review). In situ analysis of Refractory Metal Nuggets in carbonaceous chodrites. *Geochimica et Cosmochimica Acta*, .

Eisenhour, D., & Buseck, P. (1992). Transmission electron microscopy of RMNs: Implications for single-phase condensation of the refractory siderophile elements. *Meteoritics*, *27*, 217–218.

El Goresy, A., Nagel, K., Dominik, B., & Ramdohr, P. (1977). Fremdlinge: Potential presolar material in Ca-Al-rich inclusions of Allende. *Meteoritics*, *12*, 215–216.

El Goresy, A., Nagel, K., & Ramdohr, P. (1978). Fremdlinge and their noble relatives. *Lunar and Planetary Science Conference Proceedings*, *9*, 1279–1303.

Ertel, W., ONeill, H. S. C., Sylvester, P., & Dingwell, D. (1999). Solubilities of Pt and Rh in a haplobasaltic silicate melt at 1300 c. *Geochimica et Cosmochimica Acta*, *63*, 2439–2449.

Ertel, W., Walter, M. J., Drake, M. J., & Sylvester, P. J. (2006). Experimental study of platinum solubility in silicate melt to 14GPa and 2273K: implications for accretion and core formation in Earth. *Geochimica et Cosmochimica Acta*, *70*, 2591–2602.

Fegley, B., & Palme, H. (1985). Evidence for oxidizing conditions in the solar nebula from Mo and W depletions in refractory inclusions in carbonaceous chondrites. *Earth and Planetary Science Letters*, *72*, 311–326.

Forman, L., Bland, P., Timms, N., Collins, G., Davison, T., Ciesla, F., Benedix, G., Daly, L., Trimby, P., Yang, L. et al. (2016). Hidden secrets of deformation: Impact-induced compaction within a CV chondrite. *Earth and Planetary Science Letters*, *452*, 133–145.

Frondel, C. (1940). Oriented inclusions of staurolite, zircon and garnet in muscovite. skating crystals and their significance. *American Mineralogist*, *25*, 69–87.

Griffith, W. P. (2009). Melting the Platinum Group Metals. *Platinum Metals Review*, *53*, 209–215.

Griffiths, T. A., Habler, G., & Abart, R. (2016). Crystallographic orientation relationships in host–inclusion systems: New insights from large EBSD data sets. *American Mineralogist*, *101*, 690–705.

Grossman, L. (1973). Refractory trace elements in Ca-Al-rich inclusions in the Allende meteorite. *Geochimica et Cosmochimica Acta*, *37*, 1119–1140.

Grossman, L. (2010). Vapor-condensed phase processes in the early solar system. *Meteoritics & Planetary Science*, *45*, 7–20.

Hariya, Y., & Kennedy, G. (1968). Equilibrium study of anorthite under high pressure and high temperature. *American Journal of Science*, *266*, 193–203.

Harries, D., Berg, T., Langenhorst, F., & Palme, H. (2012). Structural clues to the origin of refractory metal alloys as condensates of the solar nebula. *Meteoritics & Planetary Science*, *47*, 2148–2159.

Herlach, D. M. (1994). Non-equilibrium solidification of undercooled metallic metls. *Materials Science and Engineering: R: Reports*, *12*, 177–272.

Hewins, R. H., Bourot-Denise, M., Zanda, B., Leroux, H., Barrat, J.-A., Humayun, M., Göpel, C., Greenwood, R. C., Franchi, I. A., Pont, S. et al. (2014). The Paris meteorite, the least altered CM chondrite so far. *Geochimica et Cosmochimica Acta*, *124*, 190–222.

Horan, M., Alexander, C. O., & Walker, R. (2009). Highly siderophile element evidence for early solar system processes in components from ordinary chondrites. *Geochimica et Cosmochimica Acta*, *73*, 6984–6997.

Hunt, C. P., Moskowitz, B. M., & Banerjee, S. K. (1995). Magnetic properties of rocks and minerals. In T. J. Ahrens (Ed.), *Rock Physics and Phase Relations: A Handbook of Physical Constants* (pp. 189–204). American Geophysical Union.

Inomata, K., Sawa, T., & Hashimoto, S. (1988). Effect of large boron additions to magnetically hard Fe-Pt alloys. *Journal of applied physics*, *64*, 2537–2540.

Jacob, D. E., Piazolo, S., Schreiber, A., & Trimby, P. (2016). Redox-freezing and nucleation of diamond via magnetite formation in the Earth's mantle. *Nature Communications*, *7*.

Jones, R., & Scott, E. (1996). *Chondrules and the protoplanetary disk*. Cambridge University Press.

Komatsu, M., Mikouchi, T., & Miyamoto, M. (2009). High-temperature annealing of amoeboid olivine aggregates: Heating experiments on olivine–anorthite mixtures. *Polar Science*, *3*, 31–55.

Krot, A. N., Scott, E. R., & Zolensky, M. E. (1997). Origin of fayalitic olivine rims and lath-shaped matrix olivine in the CV3 chondrite Allende and its dark inclusions. *Meteoritics & Planetary Science*, *32*, 31–49.

Lauder, W. (1961). Reaction of crystal structures and reaction fabric. *American Mineralogist*, *46*, 1317–1328.

Lauretta, D. S., Kremser, D. T., & Fegley Jr, B. (1996). The rate of iron sulfide formation in the solar nebula. *Icarus*, *122*, 288–315.

Lodders, K. (2003). Solar system abundances and condensation temperatures of the elements. *The Astrophysical Journal*, *591*, 1220–1247.

Luo, C., & Sellmyer, D. J. (1999). Structural and magnetic properties of FePt: SiO2 granular thin films. *Applied Physics Letters*, *75*.

Médard, E., Schmidt, M. W., Wälle, M., Keller, N. S., & Günther, D. (2015). Platinum partitioning between metal and silicate melts: Core formation, late veneer and the nanonuggets issue. *Geochimica et Cosmochimica Acta*, *162*, 183–201.

Mendybaev, R. A., Richter, F. M., & Davis, A. M. (2006). Crystallization of melilite from CMAS-liquids and the formation of the melilite mantle of Type B1 CAIs: Experimental simulations. *Geochimica et cosmochimica acta*, *70*, 2622–2642.

Nagahara, H., Kushiro, I., & Mysen, B. O. (1994). Evaporation of olivine: Low pressure phase relations of the olivine system and its implication for the origin of chondritic components in the solar nebula. *Geochimica et cosmochimica acta*, *58*, 1951–1963.

Palme, H., Borisov, A., & Wulf, A. (1998). Experimental determination of the oxidation sequence of refractory metals. *Lunar and Planetary Science Conference*, *29*, 1611.

Palme, H., & Wlotzka, F. (1976). A metal particle from a Ca, Al-rich inclusion from the meteorite Allende, and the condensation of refractory siderophile elements. *Earth and Planetary Science Letters*, *33*, 45–60.

Petaev, M. I., Wood, J. A., Meibom, A., Krot, A. N., & Keil, K. (2003). The ZONMET thermodynamic and kinetic model of metal condensation. *Geochimica et Cosmochimica Acta*, *67*, 1737–1751.

Piazolo, S., La Fontaine, A., Trimby, P., Harley, S., Yang, L., Armstrong, R., & Cairney, J. M. (2016). Deformation-induced trace element redistribution in zircon revealed using atom probe tomography. *Nature communications*, *7*.

Ping, L. R., Azad, A.-M., & Dung, T. W. (2001). Magnesium aluminate (MgAl2O4) spinel produced via self-heat-sustained (SHS) technique. *Materials research bulletin*, *36*, 1417–1430.

Rellinghaus, B., Stappert, S., Acet, M., & Wassermann, E. F. (2003). Magnetic properties of FePt nanoparticles. *Journal of magnetism and magnetic materials*, *266*, 142–154.

Rudraswami, N., Prasad, M. S., Plane, J., Berg, T., Feng, W., & Balgar, S. (2014). Refractory metal nuggets in different types of cosmic spherules. *Geochimica et Cosmochimica Acta*, *131*, 247–266.

Schwander, D., Berg, T., Harries, D., Schönhense, G., & Ott, U. (2014). Composition and clues to the origin of refractory metal nuggets extracted from chondritic meteorites. *Meteoritics & Planetary Science*, *49*, 1888–1901.

Schwander, D., Buhre, S., Schönhense, G., & Ott, U. (2015a). Synthesis of refractory metal nuggets and constraints on the thermal histories of nugget-bearing Ca, Al-rich inclusions. *Meteoritics & Planetary Science*, *50*, 893–903.

Schwander, D., Kööp, L., Berg, T., Schönhense, G., Heck, P., Davis, A., & Ott, U. (2015b). Formation of refractory metal nuggets and their link to the history of CAIs. *Geochimica et Cosmochimica Acta*, *168*, 70–87.

Scott, E. R., Keil, K., & Stöffler, D. (1992). Shock metamorphism of carbonaceous chondrites. *Geochimica et Cosmochimica Acta*, *56*, 4281–4293.

Sneddon, G. C., Trimby, P. W., & Cairney, J. M. (in review). Transmission Kikuchi diffraction in a scanning electron microscope: a review, .

Sylvester, P. J., Ward, B. J., Grossman, L., & Hutcheon, I. D. (1990). Chemical compositions of siderophile element-rich opaque assemblages in an Allende inclusion. *Geochimica et Cosmochimica Acta*, *54*, 3491–3508.

Trimby, P. W. (2012). Orientation mapping of nanostructured materials using transmission Kikuchi diffraction in the scanning electron microscope. *Ultramicroscopy*, *120*, 16–24.

Trimby, P. W., Cao, Y., Chen, Z., Han, S., Hemker, K. J., Lian, J., Liao, X., Rottmann, P., Samudrala, S., Sun, J. et al. (2014). Characterizing deformed ultrafine-grained and nanocrystalline materials using transmission Kikuchi diffraction in a scanning electron microscope. *Acta materialia*, *62*, 69–80.

Wang, Y., Hua, X., & WeiBiao, H. (2007). Petrogenesis of opaque assemblages in the Ningqiang carbonaceous chondrite. *Science in China Series D: Earth Sciences*, *50*, 886–896.

Wark, D. (1986). Evidence for successive episodes of condensation at high temperature in a part of the solar nebula. *Earth and planetary science letters*, *77*, 129–148.

Wark, D., & Lovering, J. (1976). Refractory/platinum metal grains in Allende calcium-aluminium-rich clasts (carc's): possible exotic presolar material? *Lunar and Planetary Science Conference*, *7*, 912.

Wasson, J., & Kallemeyn, G. (1988). Compositions of chondrites. *Philosophical Transactions of the Royal Society of London A: Mathematical, Physical and Engineering Sciences*, *325*, 535–544.

Yokoyama, T., Walker, D., & Walker, R. J. (2009). Low osmium solubility in silicate at high pressures and temperatures. *Earth and Planetary Science Letters*, *279*, 165–173.

Figure 1

Click here to download high resolution image

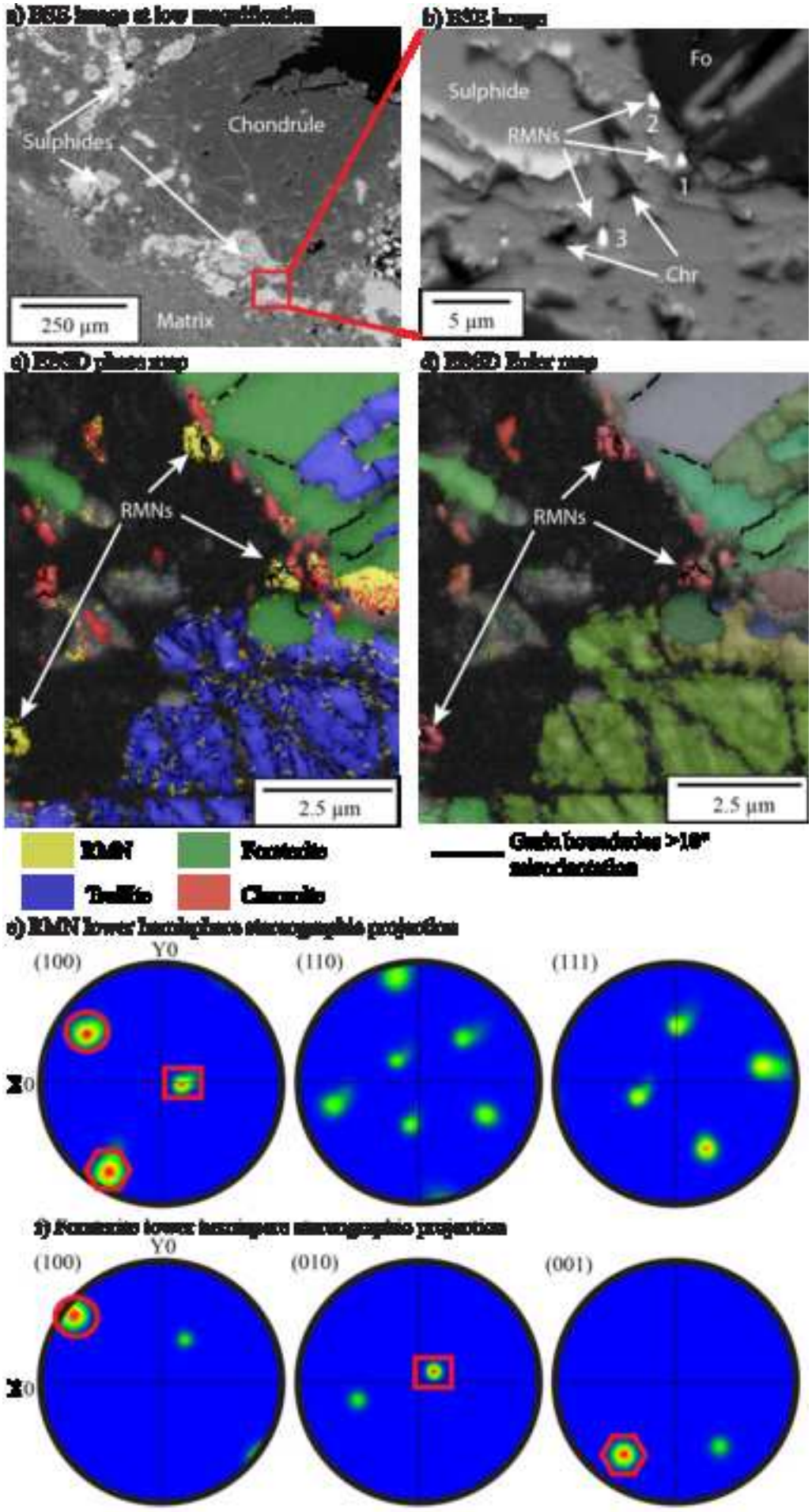

Figure 2

Click here to download high resolution image

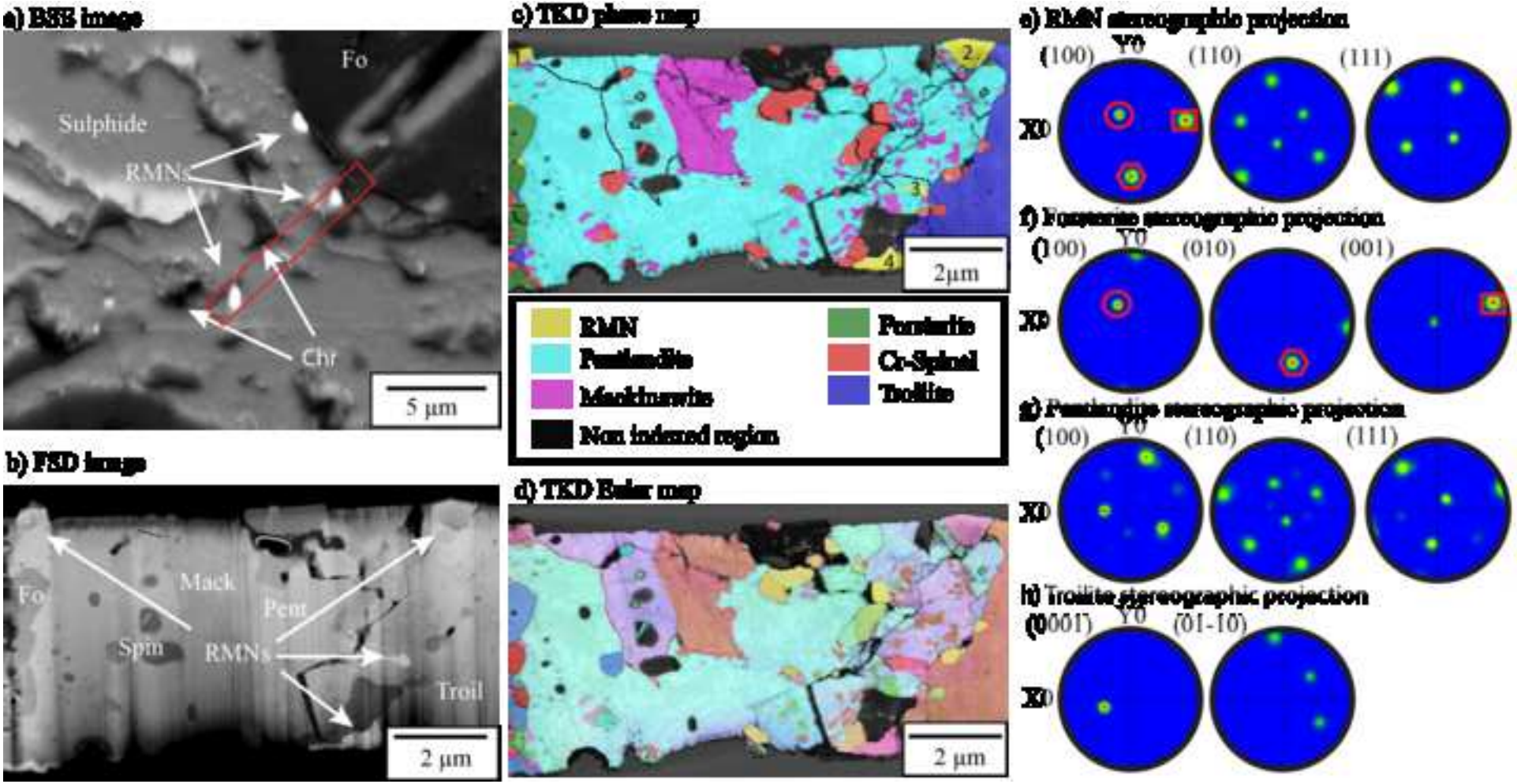

Figure 3

Click here to download high resolution image

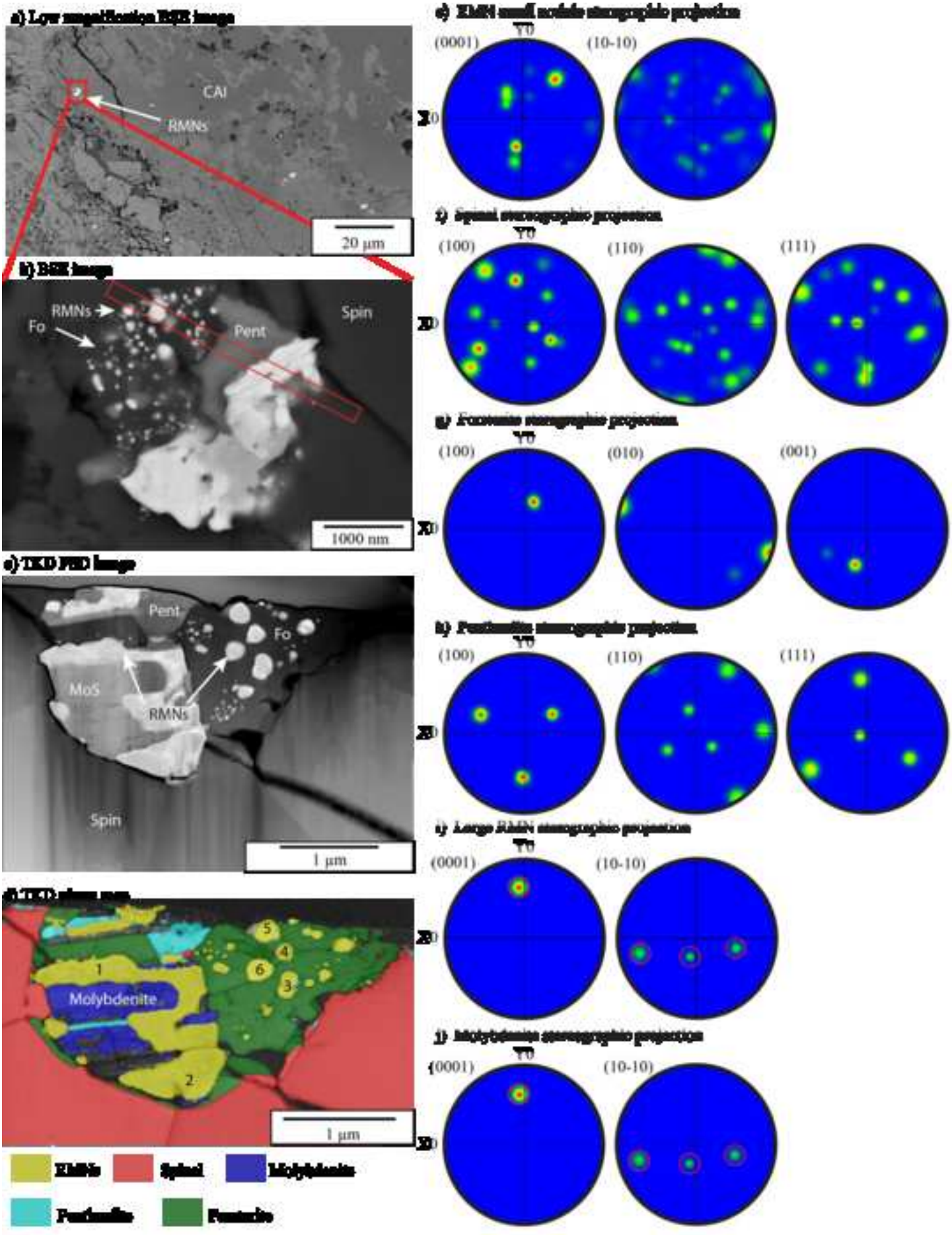

Figure 4

Click here to download high resolution image

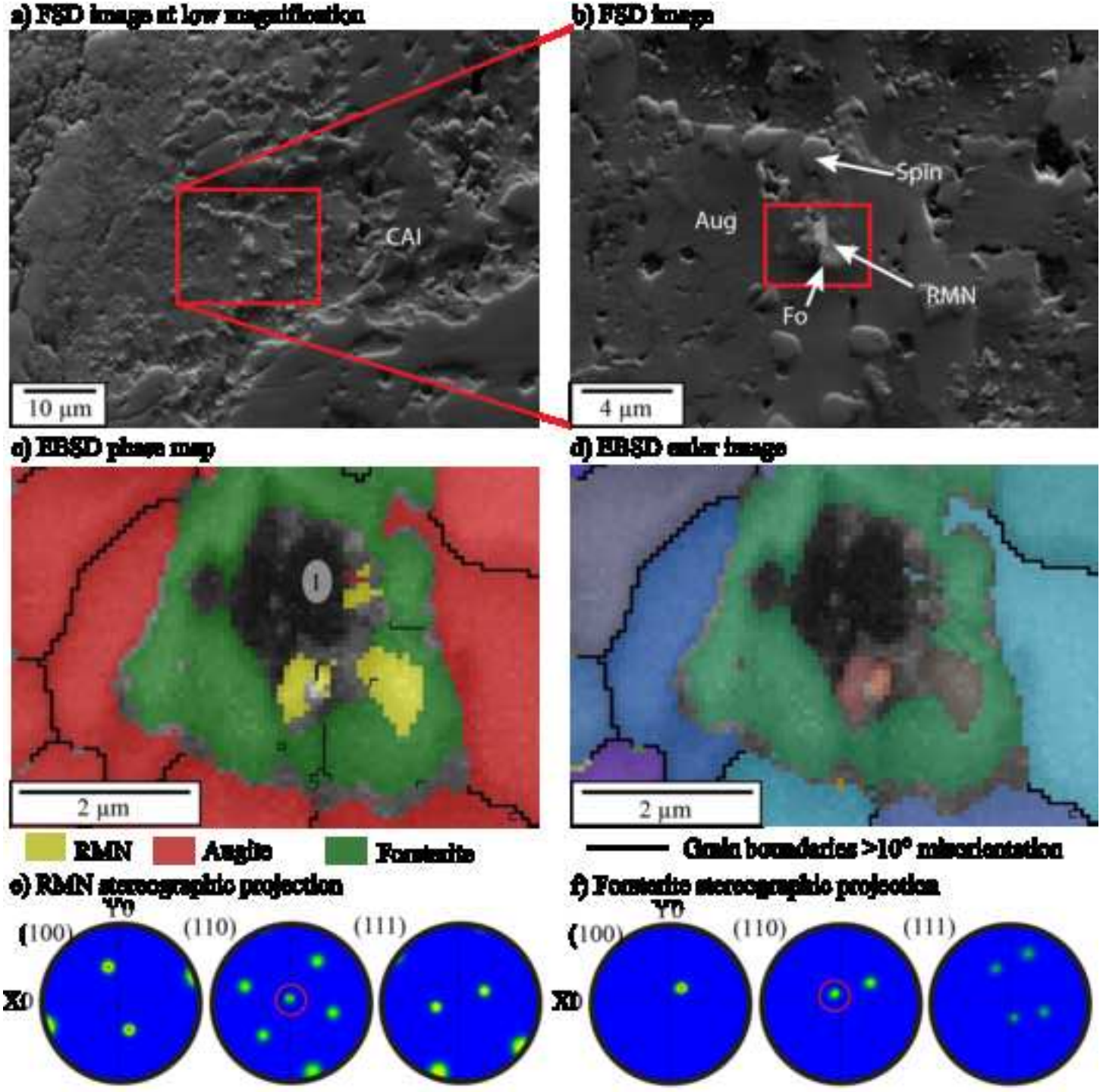

Figure 5

Click here to download high resolution image

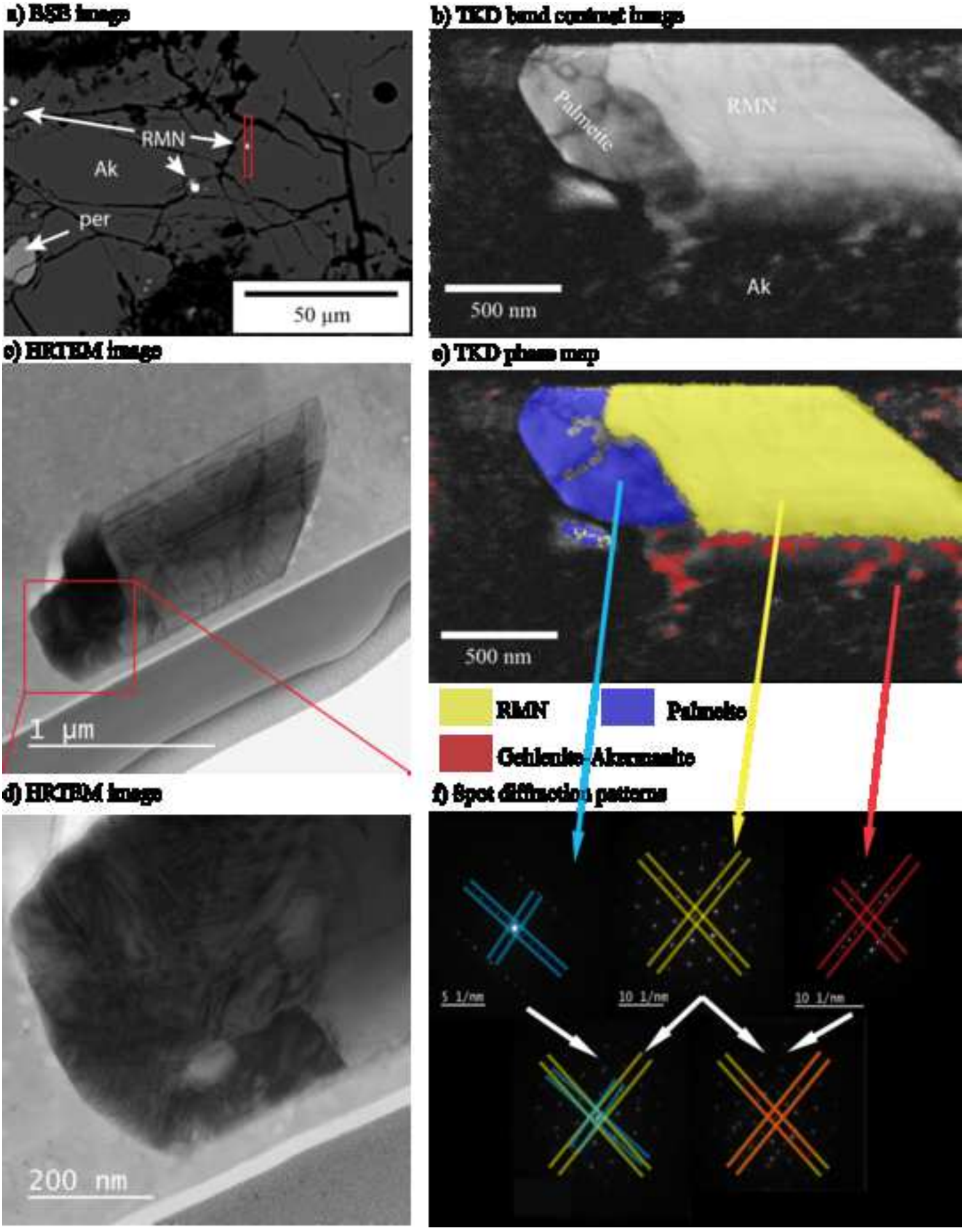

Figure 6

Click here to download high resolution image

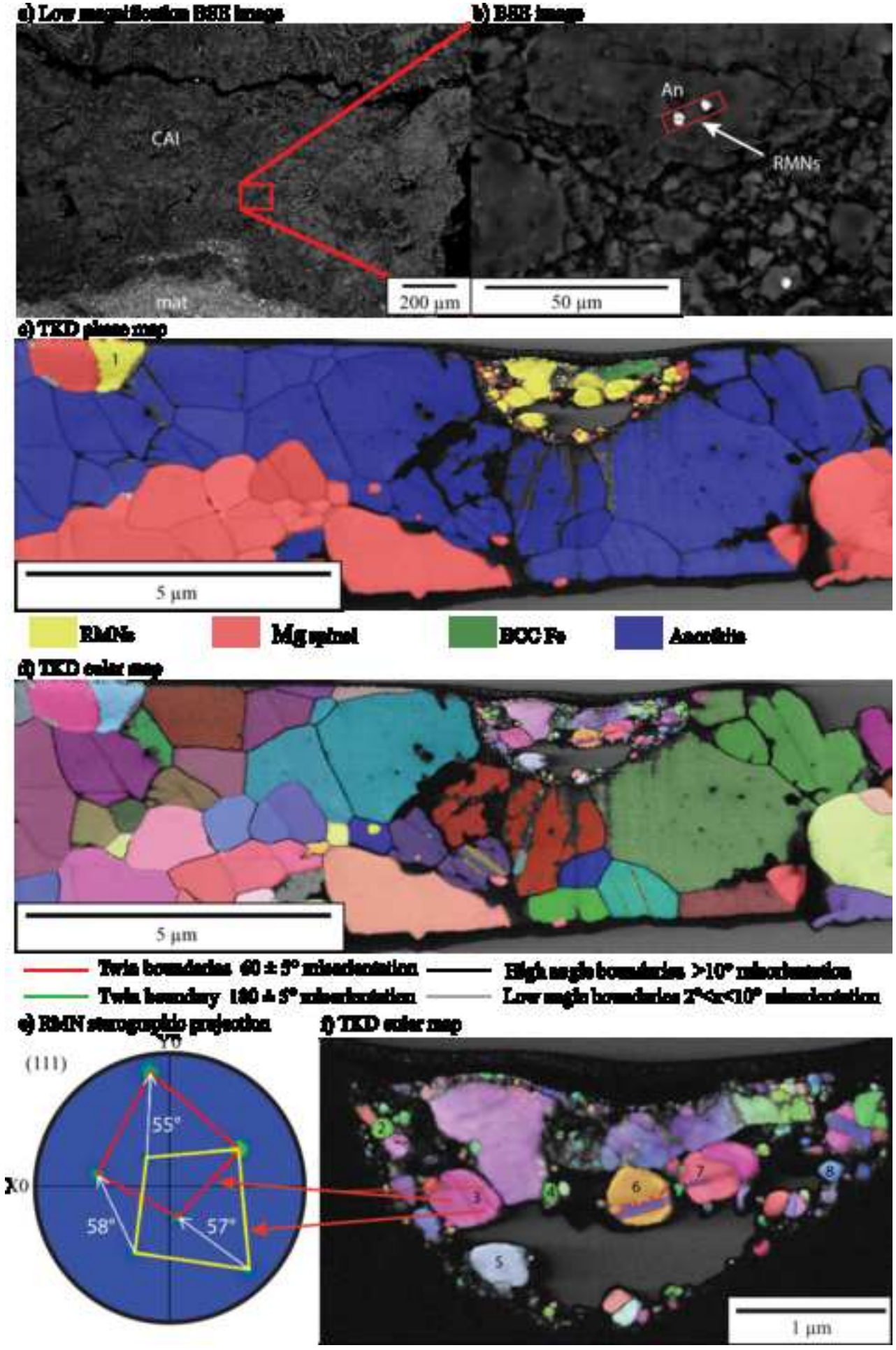

Figure 7

Click here to download high resolution image

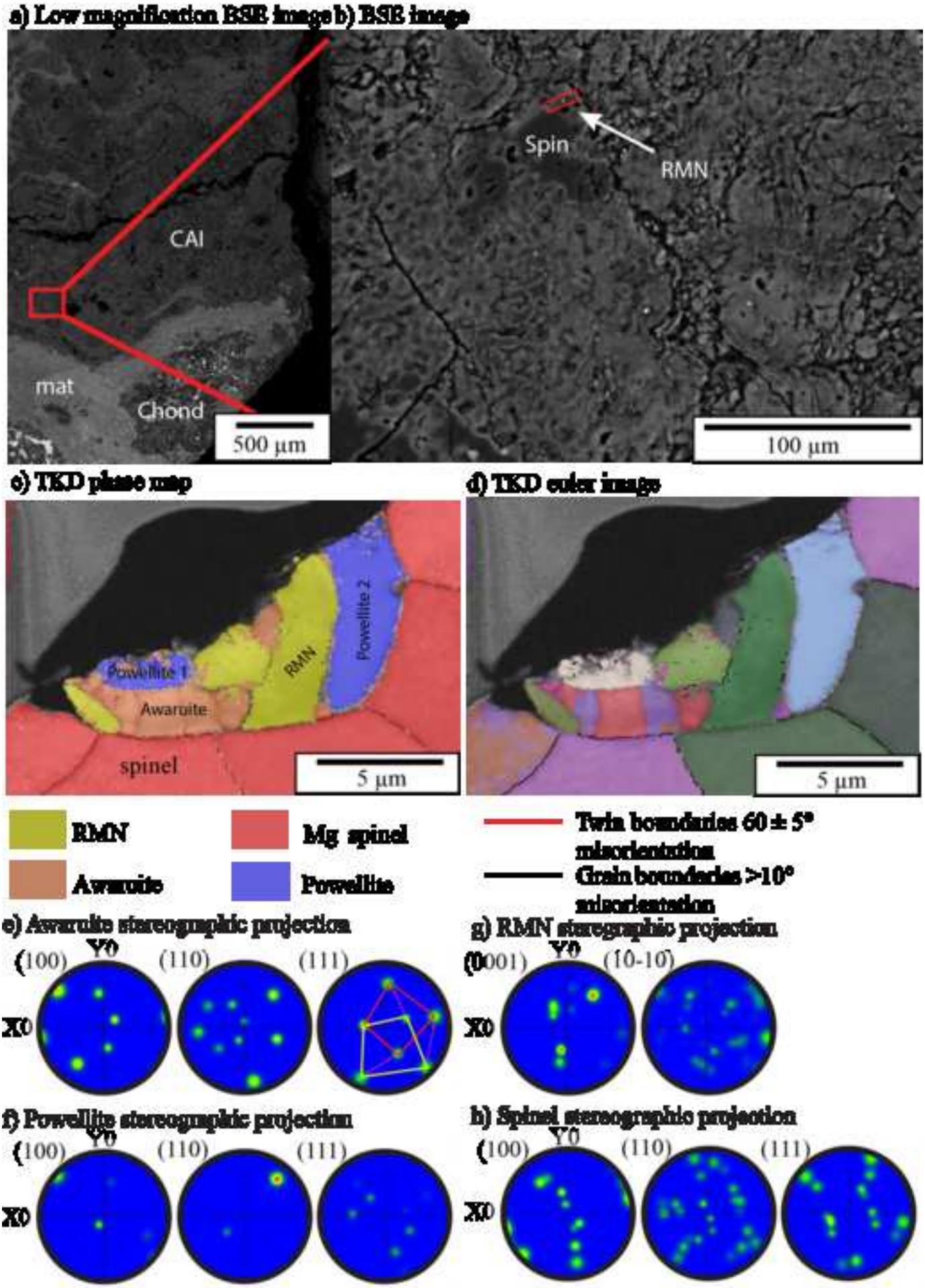

LaTeX Source Files

Click here to download LaTeX Source Files: latex source files.zip